Eur. J. Mineral., 37, 667–693, 2025
https://doi.org/10.5194/ejm-37-667-2025

European Journal of Mineralogy
Open Access

The magmatic–hydrothermal transition record in zircon: implications for zircon texture, composition and rare-metal granite dating (Beauvoir granite, French Massif Central)

Nicolas Esteves[1], Pierre Bouilhol[1], Urs Schaltegger[2], Maria Ovtcharova[2], André Navin Paul[2,3], and Lydéric France[1,4]

[1]Université de Lorraine, CNRS, CRPG, Nancy, 54000, France
[2]Department of Earth Sciences, Université de Genève, Genève, 1200, Switzerland
[3]Institute of Geosciences, Goethe University, Frankfurt am Main, Germany
[4]Institut Universitaire de France (IUF), France

Correspondence: Nicolas Esteves (nicolas.esteves@univ-lorraine.fr)

Received: 11 December 2024 – Revised: 12 June 2025 – Accepted: 17 July 2025 – Published: 7 October 2025

Abstract. Zircon petrochronology is widely used to quantify the age and duration of magma emplacement and differentiation. However, in highly differentiated magmas, such as those forming rare-metal granites, zircon may form at the magmatic–hydrothermal transition, and its primary crystallisation history, together with its secondary hydrothermal overprint, needs to be resolved and clarified. To resolve zircon formation in such evolved and mineralised granitic systems, we investigated heterogeneous zircons from the Beauvoir rare-metal granite (Massif Central, France). Most of the Beauvoir zircons are characterised by the presence of two distinct domains, designated as Zone 1 and Zone 2. Zone 1 occurs as rounded, Si- and Zr-rich domains, which are embedded in the interconnected Si- and Zr-poor Zone 2 domains that are also extremely P-, U-, F-, Ca-, Fe- and Mn-rich. Both of these zones are strongly damaged (metamict) by radioactive decay, mainly from their high U concentrations. Textures and chemical composition strongly suggest that Zone 1 corresponds to magmatic zircon that has been partly replaced by the Zone 2 material during the magmatic–hydrothermal transition. The crystallisation of Zone 1 zircon is preceded by the crystallisation of U-rich cores (~ 6 wt % UO_2) containing UO_2 (uraninite) micro-inclusions, which are then surrounded by a Zone 1 homogeneous rim. These uraninite micro-inclusions resulted from the uranium migration in the metamict and amorphous precursor zircon. U-Pb dating of single zircon grains using chemical abrasion, isotope dilution thermal ionisation mass spectrometry (CA-ID-TIMS) techniques yielded a well-defined discordia line with an upper intercept at 312 ± 2.9 (7.2) Ma (2σ) and a near-zero-age lower intercept. The discordancy reflects the continuous loss of radiogenic lead from a heavily damaged and aperiodic zircon lattice. On the other hand, ID-TIMS data from magmatic apatite of the Beauvoir granite yielded an age of 313.4 ± 0.2 (1.3) Ma (2σ), so far, the most accurate and precise crystallisation age of the Beauvoir granite. Thus, we emphasise that although the study of zircon from highly differentiated systems provides strong insights into the magmatic–hydrothermal transition of these objects, their metamict nature prevents their use to precisely and accurately date the emplacement of rare-metal granite.

1 Introduction

Peraluminous rare-metal magmatism involving highly evolved magmas is often considered to represent the ultimate stage of magmatic differentiation (e.g. Černý et al., 1985; Černý, 1992; Raimbault et al., 1995; Zoheir et al., 2020; Liu et al., 2022). This magmatism occurs as either volcanics (e.g. Pichavant et al., 1988; Raimbault and Burnol, 1998), pegmatites (e.g. Černý et al., 1985; Van Lichtervelde et al., 2007; London, 2018) or granites (e.g. Cuney et al., 1992; Michaud et al., 2020; López-Moro et al., 2024) and is of great scientific and societal importance for being a source of several critical and strategic metals (e.g. Li, Nb, Ta, Sn, W, U; see Linnen et al., 2012). As these elements are mostly incompatible with respect to the main crystallising assemblage in granitic magmas, their concentrations in highly differentiated systems (e.g. rare-metal granites, pegmatites) are governed by the various magmatic and hydrothermal processes that shape these magmatic reservoirs.

Zircon is a common mineral in granitic magmas, and it has been widely shown that it can be used to precisely monitor both the plutonic emplacement through its precise and accurate dating (e.g. Leuthold et al., 2012; Schoene et al., 2012; Barboni et al., 2013, 2015; Kryza et al., 2014; Large et al., 2020) and the subsequent magma differentiation using its composition as a proxy (e.g. Claiborne et al., 2006; Watson et al., 2006; Schoene et al., 2012; Chelle-Michou et al., 2014; Large et al., 2020; Lu et al., 2023; Drabon et al., 2024; Farina et al., 2024). In highly differentiated, peraluminous magmatic systems, zircon often exhibits textures and compositions that may be attributed to crystallisation/alteration by deuteric (i.e. melt-exsolved) fluids during the magmatic–hydrothermal transition (e.g. Černý and Siivola, 1980; Geisler et al., 2007; Schaltegger, 2007; Van Lichtervelde et al., 2009; Breiter and Škoda, 2012; Alekseev et al., 2014; Troch et al., 2018; Courtney-Davies et al., 2019; Han et al., 2023; Jia et al., 2024). Such zircons can be particularly rich in Hf and U, reflecting substitution reactions between zircon and its structural isomorphs (i.e. tetragonal crystal lattice). These substitution reactions correspond to the hafnon ($Zr^{4+} \leftrightarrow Hf^{4+}$; Ramakrishnan et al., 1969; Speer and Cooper, 1982) and the coffinite ($Zr^{4+} \leftrightarrow U^{4+}$; Fuchs and Gebert, 1958; Förster, 2006) substitutions, respectively. Zircon can also be enriched in P, reflecting the isomorphous xenotime substitution with $Si^{4+} + Zr^{4+} \leftrightarrow P^{5+} + (REE, Sc, Y)^{3+}$, where REE denotes rare-earth elements (e.g. Speer, 1980; Hoskin et al., 2000; Hanchar et al., 2001; Förster, 2006). Other elements such as Al and Ca can also be incorporated into zircon in addition to the xenotime substitution, corresponding to the berlinite substitution with $2\ Si^{4+} \leftrightarrow P^{5+} + Al^{3+}$ (e.g. Breiter et al., 2006; Pérez-Soba et al., 2014) and the brabantite substitution with $2\ Si^{4+} + 2\ Zr^{4+} \leftrightarrow 2\ P^{5+} + Ca^{2+} + (U, Th)^{4+}$ (e.g. Pérez-Soba et al., 2014; René, 2014). The berlinite and brabantite substitutions are not isomorphous with zircon.

In addition to the lattice disordering induced by these various substitutions, the zircon structure can experience significant α-decay damage due to its U and/or Th decay, ultimately leading to metamict and aperiodic zircon (Holland and Gottfried, 1955; Murakami et al., 1991; Nasdala et al., 1998, 2001; Geisler et al., 2003c) from which the radiogenic lead (Pb*) can easily escape. Although the migration of these exotic elements is enhanced by zircon α-decay damage (Cherniak et al., 1991; Geisler et al., 2003c, 2007), they can also incorporate fresh zircon (non-metamict) directly from the melt or from hydrothermal fluids. Such early incorporation would thus provide strong constraints on melt and/or fluid composition from which zircon has crystallised (e.g. Van Lichtervelde et al., 2009; Courtney-Davies et al., 2019; Han et al., 2023), which in turn can inform us about the processes related to mineralisation deposits.

To better understand these processes, we investigated the composition and crystal lattice of zircon from the Beauvoir rare-metal granite (Massif Central, France) through chemical and isotopic analysis and micro-Raman spectroscopy. Based on these new results, we show that primary magmatic zircon has been partially replaced during interactions with reactive deuteric fluids that circulated during the Beauvoir hydrothermal activity. These replacements were accompanied by changes in zircon texture and composition, which eventually led to their amorphisation. New U-Pb age determinations by CA-ID-TIMS (chemical abrasion, isotope dilution thermal ionisation mass spectrometry) reflect the advanced state of lattice damage and continuous loss of radiogenic Pb, yielding strongly discordant data with an upper intercept at 312 ± 7.2 Ma (2σ). Although our zircon data from the Beauvoir rare-metal granite provide strong insights into the Beauvoir magmatic–hydrothermal transition, we demonstrate that ID-TIMS U-Pb geochronology of magmatic apatite can yield an accurate estimation of rare-metal granite emplacement dating, which corresponds to 313.4 ± 0.2 (1.3) Ma for the Beauvoir intrusion.

2 The Beauvoir granite

2.1 Geological setting

The Beauvoir rare-metal granite is located in the Sioule area (Fig. 1), which corresponds to an inverted metamorphic sequence (Grolier, 1971) in the northern part of the Variscan Massif Central (France). The Sioule area is bordered by two major fault systems, the late Carboniferous Sillon Houiller to the west and the Oligocene Ebreuil graben to the east. From top to bottom, this metamorphic series is composed of a cordierite migmatite overlying a biotite–sillimanite gneiss, referred to as the Upper Gneiss Unit (UGU; Grolier, 1971; Faure et al., 1993). A two-mica paragneiss is located structurally below the UGU and corresponds to the Lower Gneiss Unit (LGU), whereas a staurolite-bearing micaschist is located at the base of this metamorphic series (Fig. 1; Grolier,

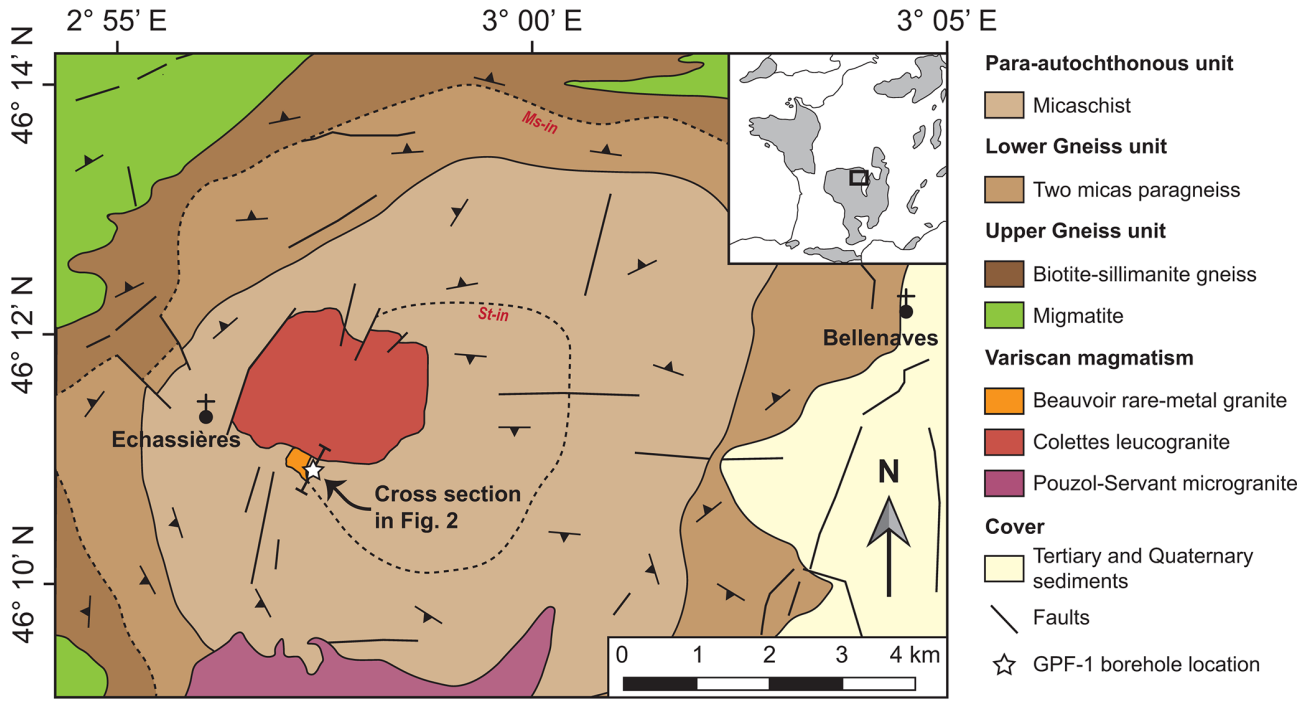

Figure 1. Geological map of the Sioule area, modified from the 1/50 000 geological map of Gannat (BRGM). The top-right insert shows the location of the Sioule area within the French Massif Central. The location of the GPF-1 borehole from which the Beauvoir samples have been collected is indicated by the open star. The location of the cross section in Fig. 2 is indicated.

1971; Faure et al., 1993). This micaschist corresponds to the Para-Autochthonous Unit. The whole series experienced a Barrovian-type metamorphism at ca. 365–350 Ma (Do Couto et al., 2016) that has been linked to the collision between Armorica and the Avalonia–Laurentia block following the closure of the Rheic Ocean (Faure et al., 2009).

The Beauvoir rare-metal granite together with the Colettes leucogranite forms the Echassières granitic complex (Fig. 1). Their intrusions into the micaschist series produced a contact aureole overprinting the regional metamorphic assemblages (Merceron et al., 1992). The Colettes leucogranite represents the main body of the Echassières complex and was emplaced at 317 ± 8 Ma (Rb–Sr whole rock from Pin, 1991, recalculated by Carr et al., 2021). The Beauvoir rare-metal granite is thought to have subsequently intruded to the Colettes leucogranite as the latter is affected by a metasomatic aureole at the contact with the Beauvoir intrusion (Aubert, 1969; Raimbault et al., 1995). Detailed studies on the Beauvoir granite fluids inclusions document an emplacement pressure of 80 MPa, corresponding to an emplacement depth of ∼ 3 km (Aïssa et al., 1987; Cuney et al., 1992). Several studies have attempted to date the Beauvoir granite crystallisation using various minerals and approaches. An age of 308 ± 2 Ma has been proposed by Cheilletz et al. (1992) using ^{40}Ar–^{39}Ar dating on lepidolite, whereas Melleton et al. (2015) estimated 317 ± 6 Ma via U-Pb on columbite–tantalite. These datings are consistent with the new Beauvoir apatite age proposed by Rocher et al. (2024) at 314.6 ± 4.7 Ma (U-Pb; LA-ICP MS). A third magma body (La Bosse), inferred to be the source of the wolframite-bearing La Bosse stockwork (Fig. 2), has been dated by Carr et al. (2021) to 316.7 ± 3.3 Ma (U-Pb on wolframite). The Sioule metamorphic series also hosts other Variscan granitoids such as the Pouzol-Servant microgranite (ca. 330 Ma; Pin, 1991; Fig. 1), the Chantelle granite, the Champs granite and late Visean volcanic deposits (ca. 330 Ma; Do Couto et al., 2016).

2.2 The Beauvoir rare-metal granite

The Beauvoir intrusion (Fig. 2) consists of a leucocratic rare-metal granite. Its mineral assemblage is composed of quartz, albite, K-feldspar, lepidolite (Li-mica), topaz and amblygonite (Li-phosphate). Accessory minerals disseminated across the granite are in order of abundance: F-apatite, cassiterite (SnO_2), columbite–tantalite (Mn–Fe, Nb–Ta_2O_6), zircon, microlite (Na–Ca_2–U, Ta_2O_6) and uraninite (UO_2). From bottom to top, the Beauvoir intrusion is characterised by an increase in incompatible element contents (e.g. Be, Li, P, F, Rb, Ta) and an overall decrease in compatible element contents (e.g. Fe, Mn, Ti, Zn). Variations of these elements are associated with a global increase in the Rb/K and the Hf/Zr ratios, which are consistent with increasing magma differentiation towards the top of the pluton (Raimbault et al., 1995; Rossi et al., 1987). Based on bulk-rock chemistry, Gagny (1987) showed that the Beauvoir intrusion resulted

from the stacking of numerous magmatic batches. A similar conclusion has been recently drawn by Esteves et al. (2024a), who showed that the Beauvoir intrusion was built through the stacking of at least 18 crystal-poor sills (i.e. sub-units in Fig. 2). Based on systematic changes in sill lepidolite composition, the authors showed that each of these sills represents residual magmas that were episodically extracted from a deeper differentiating reservoir. Once injected within the Beauvoir reservoir, the progressive crystallisation of these sills has led to the formation of Na-, Al-, Li-, P- and F-rich residual melts, which then percolated in channels through the granitic mush before its ultimate solidification.

From melting and crystallisation experiments using Beauvoir samples as starting materials, Pichavant (2022) estimated a solidus temperature of around 560 °C. Such a low solidus temperature is explained by the high volatile and Li content that strongly reduce magma solidus temperature (Wyllie and Tuttle, 1964; London, 1992; Scaillet et al., 1995). At the end of the Beauvoir magmatic activity, a hydrothermal activity occurred involving several different aqueous fluids and chlorine-rich brine stages (Aïssa et al., 1987; Fouillac et al., 1987; Harlaux et al., 2017; Rocher et al., 2024). This protracted hydrothermal activity produced a geochemical halo in rare metals in the micaschist around the Echassières granitic complex (Harlaux et al., 2025).

Zircon grains in the Beauvoir granite (size ∼ 20–80 µm) crystallised as octahedral crystals, displaying a perfect bipyramidal morphology (Fig. 3a–f). A second acicular group has been locally observed in Beauvoir units 1 and 2 (Fig. 2). Zircon is commonly enclosed in lepidolite and caused pleochroic halos in the host minerals. Those zircons are Hf-rich (up to 19.15 wt % HfO_2), reflecting the hafnon substitution, and U-rich (up to 9.69 wt % UO_2), reflecting the coffinite substitution (Breiter and Škoda, 2012). Although Breiter and Škoda (2012) analysed 31 oxides including REE, their analytical oxide sums ranged from ∼ 92 % to 100 %. They thus proposed that water might be present in these zircon grains. While metamict crystals have been ubiquitously identified across the granite, potential zircon crystals with a lower degree of α-decay damage were optically identified at various depths by Rossi et al. (1987). Three distinct apatite generations have been recognised in the Beauvoir intrusion (Rocher et al., 2024), all of them corresponding to fluoro-apatite. The first generation (Apatite I) refers to early and magmatic apatite. These prismatic grains (up to 0.5 mm) are often included in or in close relation to topaz crystals and are easily recognised with bluish colour in natural light. This magmatic generation is characterised by a high amount of manganese (up to 6.5 wt % MnO; Rocher et al., 2024), which can enter the calcium site. The incorporation of Mn is expected to explain its bluish colour (Ribeiro et al., 2005). The second and third apatite generations (Apatite II and Apatite III) crystallised during the early and late Beauvoir hydrothermal circulation events, respectively (Rocher et al., 2024). They are colourless in natural light and are depleted in manganese compared to the first generation (Cuney and Autran, 1988; Rocher et al., 2024).

3 Material and methods

Samples were collected from the 900 m GPF-1 borehole stored at the Bureau de Recherches Géologiques et Minières (BRGM; Orléans, France). Sampling was conducted at specific depths, where Rossi et al. (1987) had observed the presence of "fresh" zircons (i.e. weakly damaged), leading to a total of 12 samples (Fig. 2). Samples are labelled as "GPF-depth" (for instance GPF-352.30 was collected at a depth of 352.3 m). Zircon grain names in relation to their host samples are indicated in Table S1 in the Supplement. Rock samples were fragmented using the Selfrag Lab apparatus (i.e. high-voltage pulse fragmentation technology from SELFRAG AG, Switzerland) installed at the GeoRessources laboratory (Steval platform, Nancy, France). To efficiently allow the liberation of crystals along grain boundaries, this fragmentation was done under 120 kV, with a pulse rate of 5 Hz for a total of ∼ 100 pulses. Heavy fractions of the obtained sands, in which zircon and apatite are concentrated (along with topaz, cassiterite, columbite–tantalite and microlite), were separated from the rock light fractions (i.e. quartz, feldspar and mica) using first a shaking table at the Centre de Recherches Pétrographiques et Géochimique (CRPG; Nancy, France) and then heavy liquids (diiodomethane, density 3.32) at the Department of Earth Sciences at the University of Geneva (Switzerland). Zircon and bluish apatite were then handpicked under a binocular microscope. Zircon crystals from GPF-680.60 and GPF-598.05 (Fig. 2) were mounted in epoxy resin for micro-Raman and electron-probe analyses.

3.1 Imaging, micro-Raman and composition analyses of zircon

The backscattered electron (BSE) images were obtained using a JEOL JXA 8230 microprobe at the CRPG under 15 kV and 15 nA. Micro-Raman measurements were performed using a high-resolution LabRAM instrument (Jobin-Yvon®, Horiba) coupled to a 50× optical microscope (Olympus®) at GeoRessources laboratory (Nancy, France). Zircon spectra were obtained using a neon laser (515 nm) with a laser power of 300 mW, resulting in an energy of 30 mW at the sample surface. Slit width was 200 µm. The energy band of neon glow lamps was used for calibration. To evaluate the ν_3 (SiO_4) zircon Raman internal vibration mode, spectra were collected in the spectral interval between 843 and 1250 cm^{-1} with a spectral resolution of 2.5 cm^{-1}. Extended zircon Raman spectra were also collected between 100 and 1200 cm^{-1}. The other internal modes (ν_1, ν_2 and ν_4) that are related to Si and O vibrations within the SiO_4 tetrahedron (Dawson et al., 1971) were not analysed due to their low intensity. A spot size of 1 µm and a dwell time of 0.1 s were used to collect the

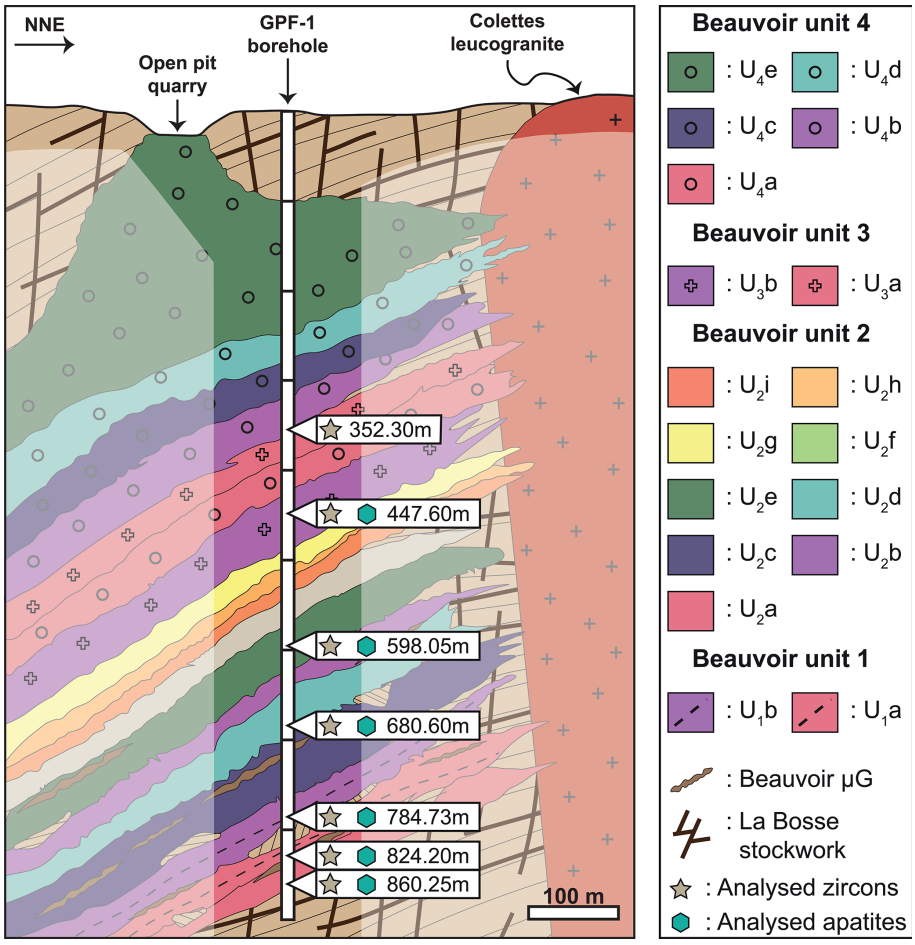

Figure 2. Schematic cross section of the Beauvoir rare-metal granite (localisation indicated in Fig. 1). Beauvoir samples from which zircon and apatite grains have been dated are indicated. The locations of the 18 sills (grouped into four main units: U_1 to U_4) identified by Esteves et al. (2024a) based on lepidolite compositional variations throughout the borehole are indicated. The shape of the whole intrusion is from Cuney et al. (1985) and redrawn by Esteves et al. (2024a).

micro-Raman maps, whereas individual micro-Raman analyses were measured with an acquisition time of 1 s, accumulated 10 times. All measurements were performed in one session. All spectra were baseline-corrected using the Labspec® software, from which the peak position and peak linewidth were calculated. Linewidth was then corrected following the equation given by Tanabe and Hiraishi (1980), which provides the real FWHM (full width at half maximum) of the Raman peak:

$$\Gamma = \Gamma_m[1 - \left(\frac{S}{\Gamma_m}\right)^2], \quad (1)$$

where Γ is the corrected linewidth, Γ_m is the measured linewidth from Labspec software and S the spectral resolution.

Following the micro-Raman measurements, both point analyses and chemical maps have been performed on an electron probe using a CAMECA SXFIVE-Tactis at the GeoRessources laboratory (Nancy, France). Each point analysis was conducted under a 10 nA current, 15 kV accelerating voltage and 1 µm diameter focused beam. Eleven element oxides were calibrated using zircon (Si, Zr), corundum (Al), $MnTiO_3$ (Mn), Fe_2O_3 (Fe), wollastonite (Ca), apatite (P), topaz (F), metallic Hf (Hf), thorium (Th) and uraninite (U). Counting times were 10 s on the peak and 5 s on the background for each element. Chemical X-ray maps were acquired under a 40 nA current, 15 kV accelerating voltage, dwell time of 50 ms and pixel size of 0.25 µm. X-ray maps were cross-calibrated with quantitative point analyses to obtain quantitative X-ray maps using XMapTools 4.2 (Lanari et al., 2014, 2019). Although the investigated zircon grains come from distinct samples, they will be treated together as their compositional analyses are overlapping. The various dark inclusions in zircon (Fig. 3a–f) have been identified and analysed using a JEOL 6510 SEM (scanning electron microscope) at the Centre de Recherches Pétrographiques et Géochimiques (Nancy, France).

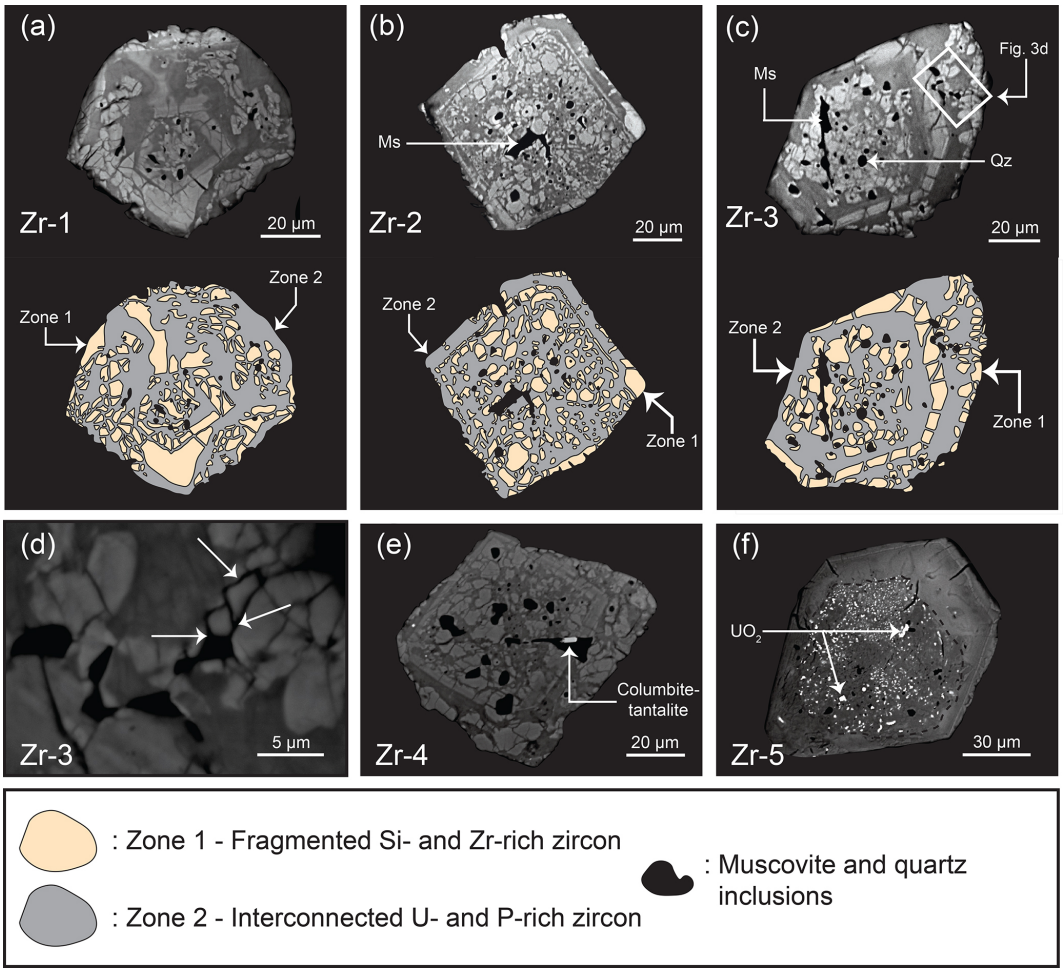

Figure 3. **(a–c)** Backscattered electron (BSE) images of representative Beauvoir zircon grains with their interpretative scheme. **(d)** Zoomed-in view of panel **(c)** presenting the connection between the Al-, Si- and K-rich inclusions and cracks (white arrows). **(e)** BSE image of Zr-4, where a small columbite–tantalite is included within an Al-, Si- and K-rich inclusion. **(f)** BSE image of Zr-5 containing a core rich in small UO_2 inclusions. Note the remarkable difference with its homogeneous rim. Zr-1, Zr-2, Zr-3, Zr-4 and Zr-5 are the names of the studied individual zircon grains.

From the U and Th concentrations, the α fluence (D_α) corresponding to the number of emitted α particles per milligram of each analysed zircon was calculated following the equation of Nasdala et al. (2001):

$$D_\alpha = 8 \times \frac{C_U \times N_A \times 0.9928}{M_{238} \times 10^9}\left(e^{\lambda^{238}t} - 1\right) + 7 \times \frac{C_U \times N_A \times 0.0072}{M_{235} \times 10^9}\left(e^{\lambda^{235}t} - 1\right) + 6 \times \frac{C_{Th} \times N_A}{M_{232} \times 10^9}\left(e^{\lambda^{232}t} - 1\right), \quad (2)$$

where C_U and C_{Th} correspond to the U and Th concentration in $\mu g\,g^{-1}$, N_A is the Avogadro constant (6.022×10^{23}), and M_{238}, M_{235} and M_{232} are the molecular weight of ^{238}U, ^{235}U and ^{232}Th, respectively. λ^{238}, λ^{235} and λ^{232} are their respective decay constants from Jaffey et al. (1971) and Le Roux and Glendenin (1963). t is the zircon crystallisation age, here 313.4 Ma (see below).

3.2 U-Pb dating of zircon and apatite

Zircon and apatite U-Pb geochronology was conducted in the Department of Earth Sciences at the University of Geneva (Switzerland). Handpicked zircon crystals separated for geochronological analyses were first annealed at 900 °C for 48 h in an oven. This annealing step allows zircons to partially recover their crystallographic structures. The annealed zircons then underwent a first washing step using ethanol before being washed a second and a third time with a 7 N HNO_3 solution with a sonic bath. Each grain was placed in Savillex microcapsules along with four drops of concentrated HF. These microcapsules were placed in a Parr bomb vessel at 210 °C for 3 h. The objective of this partial disso-

lution step is to dissolve the more strongly decay-damaged domains in the zircon that likely contain elevated contents of common lead (Pb_c). Although the optimal duration of this partial dissolution step is estimated to be 8–12 h (Widmann et al., 2019; McKanna et al., 2024), our zircon grains were already completely dissolved after 3 h. Solutions of the sample GPF-598.05 (i.e. corresponding to fully dissolved zircon) were dried before being spiked with one drop of the EARTHTIME ^{202}Pb–^{205}Pb–^{233}U–^{235}U tracer solution (Condon et al., 2015; McLean et al., 2015) together with three drops of 6 N HCl. Knowing that the Beauvoir zircons might not survive to reach the partial dissolution step, zircons from further samples, GPF-352.30, GPF-447.60, GPF-784.73, GPF-824.20 and GPF-860.25, were spiked before the dissolution step using the EARTHTIME ^{205}Pb–^{233}U–^{235}U tracer solution (Condon et al., 2015; McLean et al., 2015). These solutions were also dried before three drops of 6 N HCl were added to their respective microcapsules. All samples were dried again and re-dissolved in three drops of 3.1 N HCl. Uranium and lead elution were isolated via an anion exchange resin using HCl and H_2O. One drop of H_3PO_4 was added to the elution solution before evaporation on a hot plate.

Apatite was analysed as individual crystals or fragments, having variable size ranging from ~ 50 to ~ 200 µm. Individual fragments were washed in 3 mL Savillex beakers in an ultrasonic bath (four times, using de-ionised ultrapure water). The fragments were then transferred into individual Savillex microcapsules, along with two to three drops of 6 N HCl and 4.8 to 17.8 mg of the EARTHTIME ^{205}Pb–^{233}U–^{235}U tracer solution (Condon et al., 2015; McLean et al., 2015), before being completely dissolved at 210 °C in a Parr bomb vessel for 24 h. After dissolution, samples were dried down on a hot plate at 120 °C and re-dissolved in 1 M HBr. U and Pb were separated using a modified HBr-based single-column anion exchange chemistry (Paul et al., 2021). U and Pb for zircon and apatite chemistry were loaded separately on outgassed, zone-refined single Re filaments with a silica-gel / phosphoric acid emitter solution, modified after Gerstenberger and Haase (1997). The U and Pb isotopic compositions were measured on an Isotopx Phoenix TIMS (thermal ionisation mass spectrometer) at the Radiogenic Isotopes Laboratory, University of Geneva. Electronic baselines and ATONA calibration were conducted for 12 h each at the beginning of the analytical work. U was measured in static mode using ATONA amplifiers, with U analysed as an oxide. Pb was analysed in a mixed Faraday–Daly configuration, with ^{204}Pb measured using the Daly detector, in a one-jump setup (real-time correction, ^{204}Pb and ^{205}Pb with the Daly detector) or in peak jumping mode using only Daly detection. Measured isotopic ratios were corrected for interferences of $^{238}U^{18}O^{16}O$ on $^{235}U^{16}O_2$ using a $^{18}O/^{16}O$ composition of 0.00205, based on repeat measurements of the U500 standard. Mass fractionation of U was corrected using a double-isotope tracer with a $^{235}U/^{233}U$ ratio of 0.99506 ± 0.005. Mass fractionation of Pb was corrected using repeat analyses of the SRM 981 standard ($\alpha = 0.20 \pm 0.02$ % a.m.u.$^{-1}$ $\pm 1\sigma$ abs.). Apatite Pb analyses were corrected for laboratory blanks, which were estimated to be 0.84 ± 0.23 pg, with $^{206}Pb/^{204}Pb$ of 18.50 ± 0.74, $^{207}Pb/^{204}Pb$ of 15.58 ± 0.31 and $^{208}Pb/^{204}Pb$ of 38.17 ± 1.14, based on repeat measurements ($n = 14$) of total procedural blanks for HBr column chemistry. Initial Pb in apatite was corrected using a ^{204}Pb-based correction, with a model initial Pb isotopic composition equivalent to the Stacey and Kramers (1975) two-stage model Pb-growth curve at 300 Ma. All data were processed using the Tripoli, YourLab and Isoplot software/Excel packages (Ludwig, 1991; Bowring et al., 2011; McLean et al., 2011; Schmitz and Schoene, 2007). Thorium abundances for each apatite grain, and subsequently $Th/U_{apatite}$, were calculated using the abundance of ^{208}Pb within the crystal and the $^{206}Pb/^{238}U$ age to calculate radiogenic in-growth (McLean et al., 2011). Zircon and apatite U-Pb age uncertainties were obtained with Isoplot software (Ludwig, 1998) and are reported at the 2σ level in the format $A \pm X$ (Y), where A corresponds to the estimated age, X is analytical uncertainty associated with A and Y is the analytical uncertainty combined with the data overdispersion (i.e. MSWD).

4 Results

4.1 Zircon texture

Under BSE imaging, the Beauvoir zircons exhibit heterogeneous textures consisting of bright and dark materials (i.e. contrasting composition), identified as zircon Zones 1 and 2, respectively (Fig. 3a–c). Zircon inner parts present a mixture of small rounded pieces (up to 5 µm) of Zone 1 material embedded in the interconnected, braided Zone 2 material (Fig. 3a–c). Around these cores, zircon alternates between homogeneous dark material (Zone 2) and Zone 1 growth zones (e.g. Fig. 3c). Zone 1 growth zones contain abundant cracks (< 1 µm) that are filled by Zone 2 material. Zircon outer rims are similar to the core with the presence of rounded Zone 1 material within the Zone 2 matrix. Beauvoir zircons also contain numerous muscovite and quartz inclusions (see Table S1 and Fig. S2 in the Supplement) that appear black in BSE images (e.g. Fig. 3b, c). These inclusions are locally connected to cracks (Fig. 3d). Columbite–tantalite is also present in one of these dark inclusions (Fig. 3e). Another zircon population represented by Zr-5 (Fig. 3f) has a core containing numerous uraninite micro-inclusions (size $\sim$ 1–2 µm). The transition from core to rim is sharp as these uraninite inclusions are absent in the Zr-5 rim. BSE intensity indicates that the Zr-5 rim is composed of a denser material than the one in the core. Zircons with typical oscillatory zoning or inherited cores are absent in our sample set.

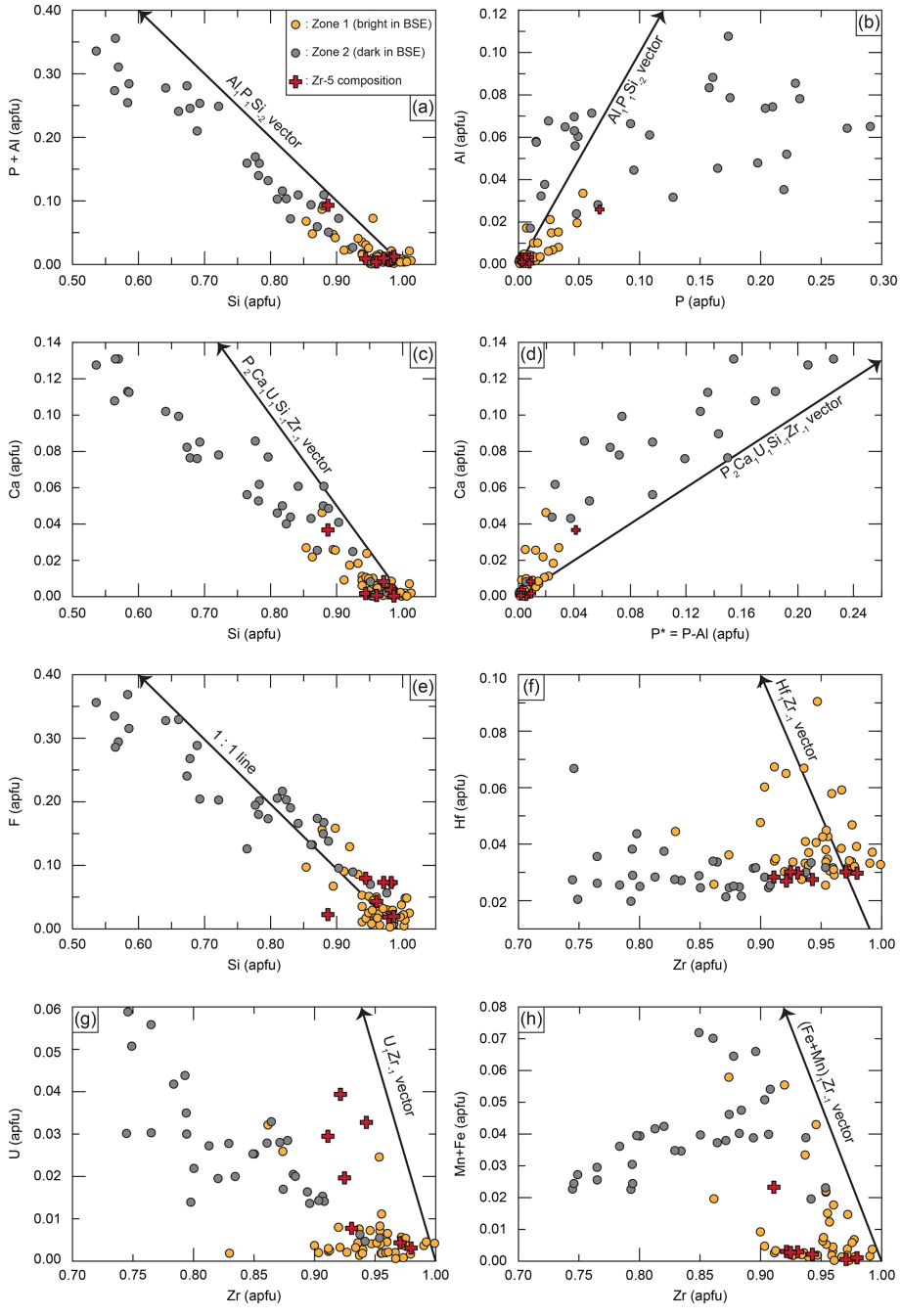

Figure 4. Compositional diagrams in atoms per formula unit (apfu) for Beauvoir zircon. **(a)** P + Al vs. Si. Note the correlation below the berlinite substitution vector. **(b)** Al vs. P. Note that Zone 2 zircon contains more P than necessary for a berlinite substitution. **(c)** Ca vs. Si. The zircon data form a linear trend below the brabantite substitution vector. **(d)** Ca vs. P*, where P* = P − Al. P* represents the leftover P after the berlinite substitution. Note the correlation along the brabantite substitution vector. **(e)** F vs. Si. Note the negative correlation along a 1 : 1 trend. **(f)** Hf vs. Zr. Note that the data do not follow the hafnon substitution vector. **(g)** U vs. Zr. Note the negative correlation below the coffinite substitution vector. **(h)** Fe + Mn vs. Zr. The black arrow corresponds to the theoretical substitution $Zr^{4+} \leftrightarrow 2\,(Fe^{2+} + Mn^{2+})$. In general, note the compositional variations between Zones 1 and 2. Also note that except its higher U content, Zr-5 is compositionally similar to Zone 1.

Table 1. Representative chemical composition and structural formula of the Beauvoir zircons. Structural formulas are calculated on the basis of two cations and four oxygens and are given in apfu (atoms per formula unit). Elements that are enriched in Zone 2 compared to Zone 1 are in bold. See the Supplement for the whole data set (Table S1) and for the location of each analysis (Fig. S1). 0.0 analyses are below the detection limit.

	Zone 1 ($n = 51$)				Zone 2 ($n = 37$)				Detection limits (DLs)
	Mean	Max	Min	SD	Mean	Max	Min	SD	wt %
SiO_2 (wt %)	30.41	32.86	25.58	1.69	23.23	31.58	16.56	4.43	0.13
Al_2O_3	0.16	1.61	0.00	0.27	**1.25**	2.69	0.00	0.68	0.11
FeO	0.22	1.72	0.00	0.40	**0.78**	2.10	0.00	0.57	0.13
MnO	0.08	0.47	0.00	0.10	**0.47**	1.08	0.00	0.26	0.13
CaO	0.20	1.26	0.00	0.26	**1.73**	3.69	0.00	1.04	0.06
P_2O_5	0.40	1.83	0.00	0.42	3.69	10.06	0.11	3.13	0.33
ZrO_2	61.68	65.83	51.48	2.61	51.98	64.84	39.05	5.80	0.25
HfO_2	4.30	9.99	2.63	1.45	3.10	6.45	2.04	0.79	0.45
ThO_2	0.00	0.00	0.00	0.00	0.00	0.00	0.00	0.00	0.22
UO_2	0.97	5.44	0.00	1.19	**3.31**	7.80	0.45	1.93	0.25
F	0.40	1.51	0.00	0.39	**1.81**	3.58	0.19	0.91	0.73
Total	98.82				91.34				
α doses (10^{16} mg^{-1})	0.85				2.95				
Number of ions on the basis of four oxygens									
Four-coordinated cations (T site)									
Si (apfu)	0.96	1.01	0.85	0.04	0.78	0.98	0.54	0.13	
Al	0.01	0.06	0.00	0.01	**0.05**	0.11	0.00	0.03	
P	0.01	0.05	0.00	0.01	**0.11**	0.29	0.00	0.09	
Sum	0.98				0.94				
Eight-coordinated cations (A site)									
Fe (apfu)	0.01	0.05	0.00	0.01	**0.02**	0.06	0.00	0.02	
Mn	0.00	0.01	0.00	0.00	**0.01**	0.03	0.00	0.01	
Ca	0.01	0.05	0.00	0.01	**0.06**	0.13	0.00	0.04	
Zr	0.95	1.00	0.86	0.03	0.85	0.98	0.68	0.07	
Hf	0.04	0.09	0.02	0.01	0.03	0.07	0.02	0.01	
Th	0.00	0.00	0.00	0.00	0.00	0.00	0.00	0.00	
U	0.01	0.04	0.00	0.01	**0.03**	0.06	0.00	0.02	
Sum	1.01				1.00				
Anionic site									
F	0.04	0.16	0.00	0.04	**0.19**	0.37	0.02	0.10	

4.2 Zircon electron-probe and micro-Raman analyses

Representative compositions of the Beauvoir zircons are documented in Table 1, while compositional variations between Zones 1 and 2 are represented in Fig. 4. Compositional variations of Zr-3 and Zr-1 are compared to their BSE images in Figs. 5 and 6, respectively. From Zone 1 and 2 compositions, several types of ionic substitution can be identified, allowing the incorporation of various elements in these zircons.

1. *"Berlinite" substitution* [$2\ Si^{4+} \leftrightarrow P^{5+} + Al^{3+}$]. Zone 1 corresponding to the bright material in BSE images is enriched in Si compared to Zone 2, with an average of 30.41 wt % and 23.23 wt % SiO_2, respectively (Figs. 4a, 5a, b and 6a, b). Cracks are also depleted in Si. For comparison, pure zircon (i.e. $ZrSiO_4$) has 32.8 wt % SiO_2 (Hoskin and Schaltegger, 2003). Si in the Zone 1 zircon T site decreases to 0.85 apfu (i.e. 25.58 wt % SiO_2) and to 0.54 apfu Si (i.e. 16.56 wt % SiO_2) in Zone 2 (Fig. 4a; Table 1). Si negatively correlates with P + Al (Fig. 4a) and forms a linear trend slightly below the berlinite substitution vector. This substitution is clearly visible in the chemical maps where Si-rich materials (Zone 1) are depleted in P and vice versa (Figs. 5b, f and 6b, f). The extent of berlinite sub-

stitution is limited in Zone 1 compared to Zone 2, leading to a Zone 1 T site almost exclusively filled with Si, while, on average, 0.05 apfu Al (1.25 wt % Al_2O_3) and 0.11 apfu P (3.69 wt % P_2O_5) enter the Zone 2 T site. As the berlinite substitution involves the incorporation of 1 P^{5+} and Al^{3+} instead of 2 Si^{4+}, the enrichment in P over Al in the Beauvoir zircons (Fig. 4b) implies that P^{5+} was also incorporated by another substitution.

2. *"Brabantite" substitution* [$2\ Si^{4+} + 2\ Zr^{4+} \leftrightarrow Ca^{2+} + (U^{4+}) + 2\ P^{5+}$]. Ca in Beauvoir zircon negatively correlates with Si, forming a linear trend below the brabantite substitution vector (Fig. 4c). On average, Ca is enriched in Zone 2 compared to Zone 1 (1.73 wt % vs. 0.20 wt % CaO, respectively; Table 1). Zircon data are slightly above the brabantite substituting vector when Ca is plotted against P*, with P* = P − Al (apfu) represents the extra P^{5+} that needs to be charge-balanced after the berlinite substitution (Fig. 4d).

3. *Incorporation of F.* Zone 2 is particularly rich in F (Fig. 4e), with an average composition of 1.81 wt % F and a maximum of 3.58 wt % F, whereas it is poorer in Zone 1 (mean of 0.4 wt % F, where most of the analyses are below the detection limit; Table 1). F negatively correlates with Si, forming a linear trend with a 1 : 1 slope in this chemical space (Fig. 4e).

4. *Hafnon substitution.* Zr, which is the main constituent in zircon, is enriched in Zone 1 compared to Zone 2 (Figs. 4f–h, 5c and 6c). On average, Zone 1 contains 61.68 wt % ZrO_2 (0.95 Zr apfu), while Zone 2 contains 51.98 wt % ZrO_2 (0.85 apfu). Although Hf does not correlate with Zr in Beauvoir zircon (Fig. 4f), the highest Hf concentration has been found in Zone 1 (9.99 wt % HfO_2; Table 1). From zircon chemical maps, Hf-rich areas (e.g. arrow in Fig. 6d) are also enriched in Si and Zr.

5. *Incorporation of U.* U negatively correlates with Zr (Fig. 4g) and is, on average, depleted in Zone 1 compared to Zone 2 (0.97 wt % vs. 3.31 wt % UO_2; Table 1). The U–Zr covariation is well below the coffinite substitution vector ($Zr^{4+} \leftrightarrow U^{4+}$, Fig. 4g). U strongly correlates with P (Figs. 5e, f and 6e, f), whereas it also negatively correlates with Si (Figs. 5b, c, e and 6b, c, e). The Th concentration in Beauvoir zircon is generally below the detection limit (Table 1).

6. *Incorporation of low-field-strength cations Mn and Fe.* Unusual elements for a zircon such as Fe and Mn are enriched in Zone 2 (0.78 wt % FeO and 0.47 wt % MnO, respectively) compared to Zone 1, where most of the analyses are below the detection limits (Table 1). For zircon containing more than 0.90 apfu Zr, Mn + Fe negatively correlates with Zr, in agreement with the theoretical $Zr^{4+} \leftrightarrow Mn^{2+} + Fe^{2+}$ substitution vector (Fig. 4h). For a Zr below 0.90 apfu, Mn + Fe does not correlate with Zr (Fig. 4h).

The oxide sum is on average 98.82 in Zone 1, while it is 91.34 wt % in Zone 2 (Table 1). Although the zircon A site is fully occupied in Zones 1 and 2, this Zone 2 low oxide sum is notably explained by a cation deficiency in its T site (0.94 instead of 1 apfu). Such a low oxide sum in Beauvoir Zone 2 may indicate the non-dosage of various elements (such as H_2O). Zr-5, displayed in Fig. 3f, is texturally different from the other Beauvoir zircons but is compositionally similar to Zone 1.

These results are consistent with the previously published Beauvoir zircon analyses by Cuney and Autran (1988) and Breiter and Škoda (2012). A comparison between the Zr-1 micro-Raman signature of Zones 1 and 2 with its chemical maps is presented in Fig. 6a–i. Although the Raman intensity is rarely used as a discriminating parameter in Raman spectroscopy (i.e. the intensity is often labelled in arbitrary units), it strongly correlates with zircon SiO_2 and ZrO_2 concentrations (Fig. 6b, c and g) and can thus be used to identify Zone 1 zircon. In other words, the decrease in Raman intensity is correlated with the substitutional degree of the analysed material. The ν_3 (SiO_4) linewidth of Zr-1 is negatively correlated with its ν_3 (SiO_4) intensity (Fig. 6g, h) as well as with SiO_2, ZrO_2 and HfO_2. On the other hand, it correlates with UO_2 and P_2O_5 concentrations, leading to a lower ν_3 (SiO_4) linewidth for Zone 1 compared to Zone 2 ($\sim$ 15 to 25 vs. 30 to 40, respectively, Fig. 6h). The Beauvoir zircons' ν_3 (SiO_4) linewidth negatively correlates with their ν_3 (SiO_4) peak position (Fig. 7a). Analyses leading to ν_3 (SiO_4) linewidths below 25 cm^{-1} exclusively refer to Zone 1, whereas an overlap exists between Zones 1 and 2 above 25 cm^{-1} (Fig. 7a). Although their ν_3 (SiO_4) linewidth correlates, in the first order, with the α decays mg^{-1} they experienced, two trends can be distinguished in the diagram (Fig. 7b). Indeed, the slope of these trends significantly differs from Zone 1 to Zone 2, with a weaker one for Zone 1 (Fig. 7b). Thus, although Zones 1 and 2 can have a similar ν_3 (SiO_4) linewidth, the α decays mg^{-1} that experienced Zone 2 are 2 to 6 times higher than those that experienced Zone 1 (Fig. 7b). Typical extended Beauvoir zircon Raman spectra are displayed in Fig. 7c and can be compared with the spectrum of a non-damaged zircon (RRUFF database; Lafuente et al., 2015). Zircon spectra with the weaker ν_3 (SiO_4) linewidth are those where the zircon Raman bands are the best expressed (e.g. little disordered Zone 1; Fig. 7c). On the other hand, ν_1 and ν_3 (SiO_4) cannot be distinguished on the Zone 2 metamict zircon spectrum (Fig. 7c). During this study, any micro-Raman analyses yielded to very well ordered zircon with a ν_3 (SiO_4) linewidth below 10 cm^{-1}.

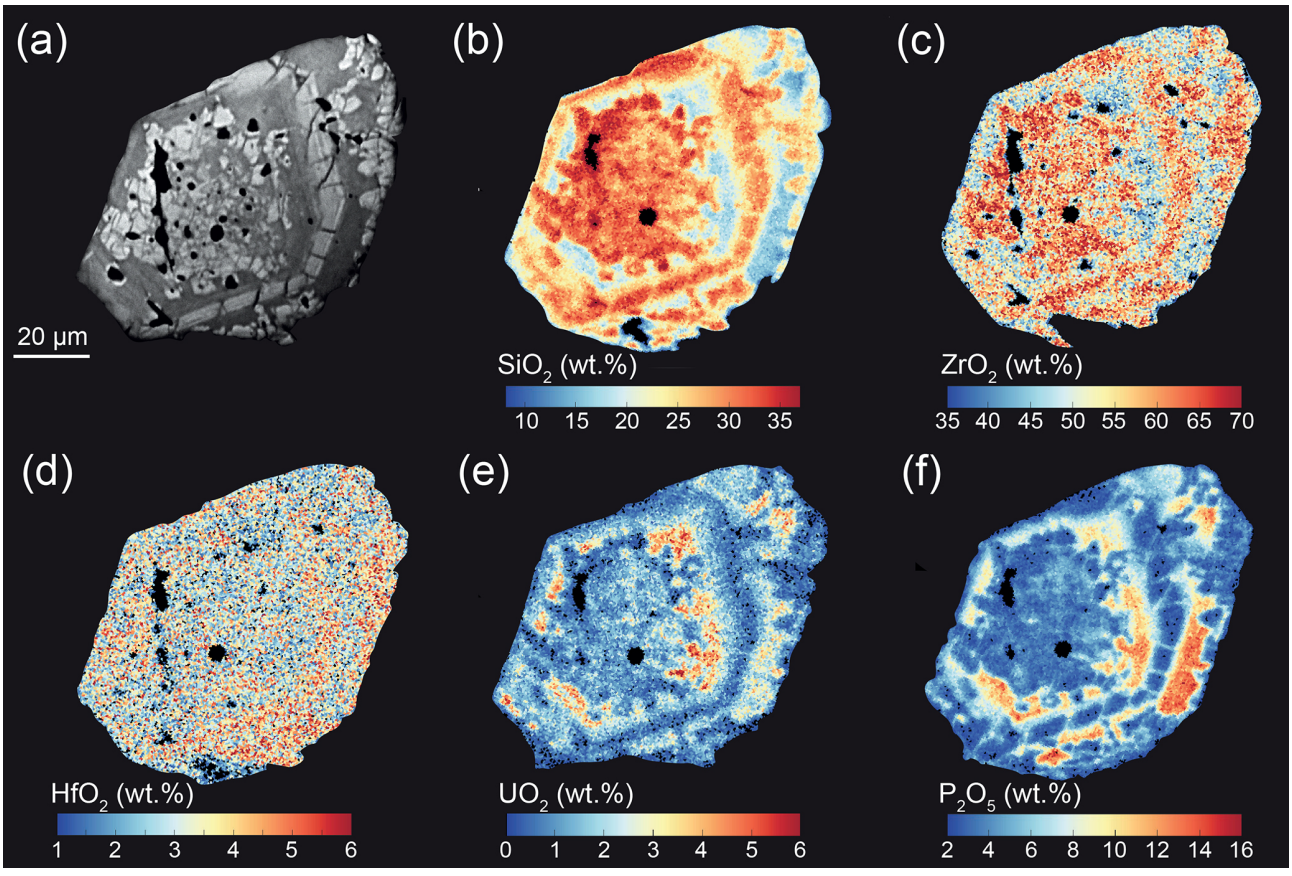

Figure 5. **(a)** BSE image of Zr-3. **(b)** SiO_2, **(c)** ZrO_2, **(d)** HfO_2, **(e)** UO_2 and **(f)** P_2O_5 quantitative chemical maps of the same crystal in **(a)**. Note that the bright domains (Zone 1) in **(a)** are enriched in Si and Zr, whereas the dark domains in **(a)** are enriched in U and P.

4.3 Zircon and apatite geochronology

All analysed Beauvoir zircons are discordant and contain variable amounts of common lead (Pb_c), ranging from 0.74 to 82.8 pg (see Table S1 in the Supplement). Analyses with a high uncertainty (i.e. large ellipse in Fig. 8a) are those with a high Pb_c/Pb^* ratio (greater than 1), whereas more precise analyses are those with smaller ellipses and a low Pb_c/Pb^* ratio. Therefore, although the Beauvoir granite is composed of several magmatic batches (Fig. 2; e.g. Gagny, 1987), all analysed zircons have been grouped together because the precision of each discordia regression line does not allow us to distinguish different magma batches. Despite their discordant nature, all zircons (except one grain) are aligned along a single discordia line, which indicates an upper-intercept age of 312.0 ± 2.9 (7.2) Ma (2σ). The lower intercept of the discordia line is near the zero age at 4.1 ± 1.4 (3.7) Ma (Fig. 8a). Of the 37 grains analysed, none provided an age older than the expected Variscan age of the Beauvoir granite.

Uranium–lead analyses of apatite yielded concordant $^{206}Pb/^{238}U$ ages, after initial Pb correction using a Stacey and Kramers (1975) two-stage model Pb evolution curve composition at 300 Ma, ranging from 362.7 ± 0.6 to 295.7 ± 0.6 Ma (Fig. 8b). Apatite grains are quite radiogenic ($^{207}Pb/^{206}Pb < 0.2$), making the choice of initial Pb composition less relevant to most analyses considering the uncertainty in the individual dates calculated. One strongly discordant apatite yielded a $^{206}Pb/^{238}U$ age of 702 ± 2 Ma, while two other discordant apatite analyses yielded $^{206}Pb/^{238}U$ ages of 313 ± 5 and 166.0 ± 0.5 Ma. These discordant apatite analyses will not be further discussed in this contribution. In order to date the Beauvoir intrusion emplacement, concordant apatite analyses yielding an age between 309 and 318 Ma were retained (the selected concordant apatite cluster in Fig. 8b), as this time interval is consistent with the previous dating performed on the Beauvoir granite (Cheilletz et al., 1992; Melleton et al., 2015; Rocher et al., 2024). These selected concordant apatite grains give a concordia age of 313.4 ± 0.2 (1.3) Ma (Fig. 8b). When plotted in the Tera–Wasserburg space, these selected concordant apatite grains (uncorrected for initial Pb) may give a date of 307.3 ± 6.2 Ma (Supplement; Fig. S3), overlapping with the $^{206}Pb/^{238}U$ concordia age. Therefore, the $^{206}Pb/^{238}U$ age at 313.4 ± 0.2 (1.3) Ma obtained from the selected and Pb_c-corrected apatite cluster will be preferred in this paper. As for the zircon analyses, the apatite measurement accuracy is controlled by

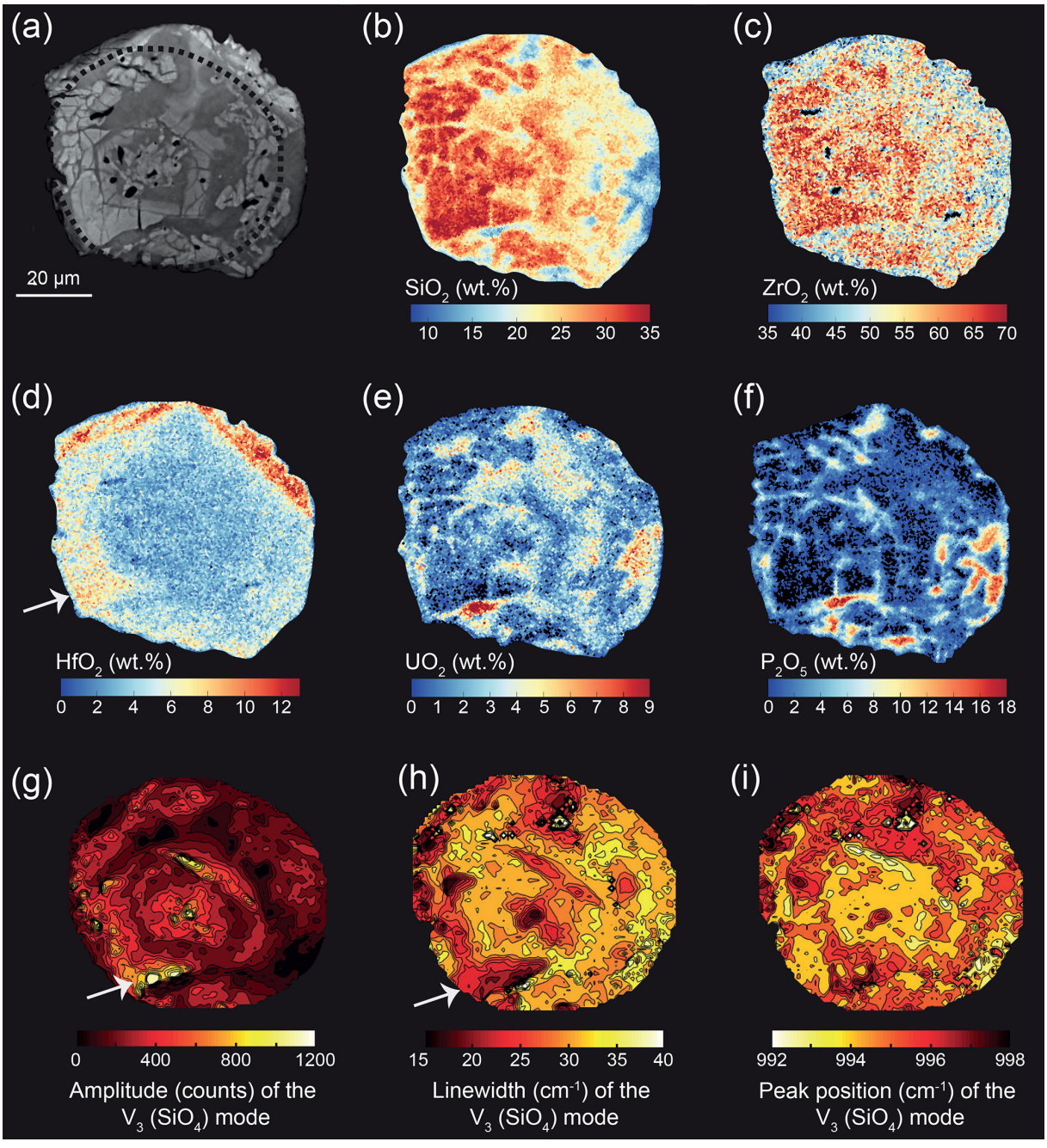

Figure 6. **(a)** BSE image of Zr-1. **(b)** SiO_2, **(c)** ZrO_2, **(d)** HfO_2, **(e)** UO_2 and **(f)** P_2O_5 quantitative chemical maps of the same crystal in **(a)**. **(g, h, i)** Raman contour maps of the area indicated by the dotted black circle in **(a)**. **(g)** ν_3 (SiO_4) intensity (counts), **(h)** ν_3 (SiO_4) linewidth (cm^{-1}) and **(i)** ν_3 (SiO_4) peak position (cm^{-1}). Note that the Si-, Zr-, and Hf-rich area indicated by the white arrow is characterised by a higher ν_3 (SiO_4) intensity and a lower ν_3 (SiO_4) linewidth.

their Pb_c/Pb^* ratio, where the more accurate analyses are those with a weak Pb_c/Pb^* (Fig. 8b). Overall, the resulting age is similar for zircon and apatite within the uncertainty.

5 Discussion

5.1 Origin of the Beauvoir zircon

5.1.1 Zone 1: a magmatic origin

The Beauvoir zircon crystals are composed of two distinct domains: Zone 1 is characterised by both rounded isolated

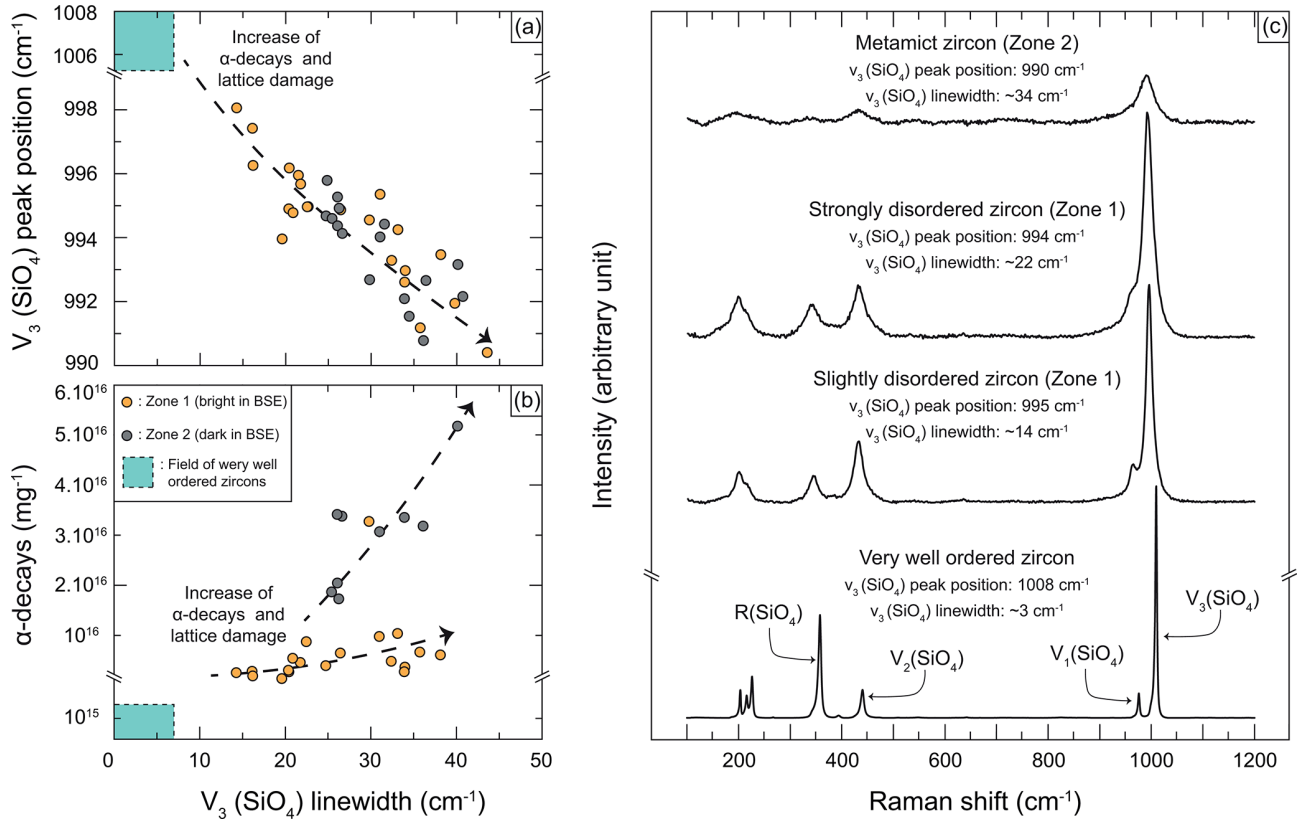

Figure 7. **(a)** Peak position (cm^{-1}) versus linewidth (cm^{-1}) of the ν_3 (SiO_4) Zone 1 and 2 Raman band. **(b)** Calculated α decays(mg^{-1}) experienced by Zones 1 and 2 versus their ν_3 (SiO_4) Raman band linewidth (cm^{-1}). Note that in **(a)** and **(b)**, the y scale is truncated to observe the field of ideal undamaged zircons (from Geisler et al., 2006). **(c)** Extended zircon Raman spectra from very well ordered to metamict zircon. The very well ordered zircon spectrum is from the RRUFF database (Lafuente et al., 2015), whereas little and strongly disordered spectra correspond to Zone 1 and the metamict spectrum corresponds to Zone 2. Note that the lattice ordering degree is strongly related to peak linewidth.

pieces within Zone 2, as well as continuous growth zones that are eventually primary (e.g. Fig. 3c). The Zone 1 fourfold site (T site) is almost exclusively occupied by Si, whereas the eightfold site (A site) is filled by Zr together with minor Hf (Table 1). The hafnon substitution is commonly observed in zircon from differentiated bodies (Neves et al., 1974; Wark and Miller, 1993; Breiter et al., 2006; Claiborne et al., 2006; Abdalla et al., 2009; Van Lichtervelde et al., 2009; Wang et al., 2010; Breiter and Škoda, 2012). The relatively high hafnium concentration and variations in the Zr/Hf ratio in Zone 1 likely reflect the parental melt composition or changes in crystallisation kinetics (e.g. dendritic growth; Gillespie et al., 2024). From their experimental work, Linnen and Keppler (2002) showed that Hf is less compatible in zircon, leading to a decrease in the Zr/Hf of the residual melt and an increase in Hf concentration in zircon during fractionation. Therefore, the relatively high hafnium concentration in Beauvoir zircon would be related to the highly differentiated nature of the Beauvoir magmas, whereas the Zr/Hf variations in each crystal would be the result of zircon growth from magmas at different degrees of differentiation (e.g. Claiborne et al., 2006).

As U was also incorporated in significant amounts (on average 0.97 wt % UO_2; Table 1) during zircon crystallisation, its protracted disintegration progressively damaged the crystal structure of Zone 1 to form strongly disordered crystals. Although the average α dose experienced by Zone 1 ($8.5 \times 10^{15} \alpha$ decays mg^{-1}) is higher than the limit of $8 \times 10^{15} \alpha$ decays mg^{-1} that defines a complete aperiodic crystal (Murakami et al., 1991), the high ν_3 (SiO_4) intensity and relatively low ν_3 (SiO_4) linewidth ($< 20\,cm^{-1}$; Figs. 6h and 7a–c) of some Zone 1 zircons strongly suggest that the crystal lattice of these zircons is only weakly to moderately disordered. On the other hand, Zone 1 zircon with high ν_3 (SiO_4) linewidth (above $25\,cm^{-1}$; Figs. 6h and 7a–c) eventually corresponds to metamict zircon. Thus, Zone 1 corresponds to both weakly to moderately damaged zircon and metamict/aperiodic zircon, an evolution that is represented by the linear trend in Fig. 7b. Taking Zone 1 zircon as a whole, we would estimate an amorphous fraction of ~ 80 % for Zone 1 zircon from the relationship between the α dose experienced

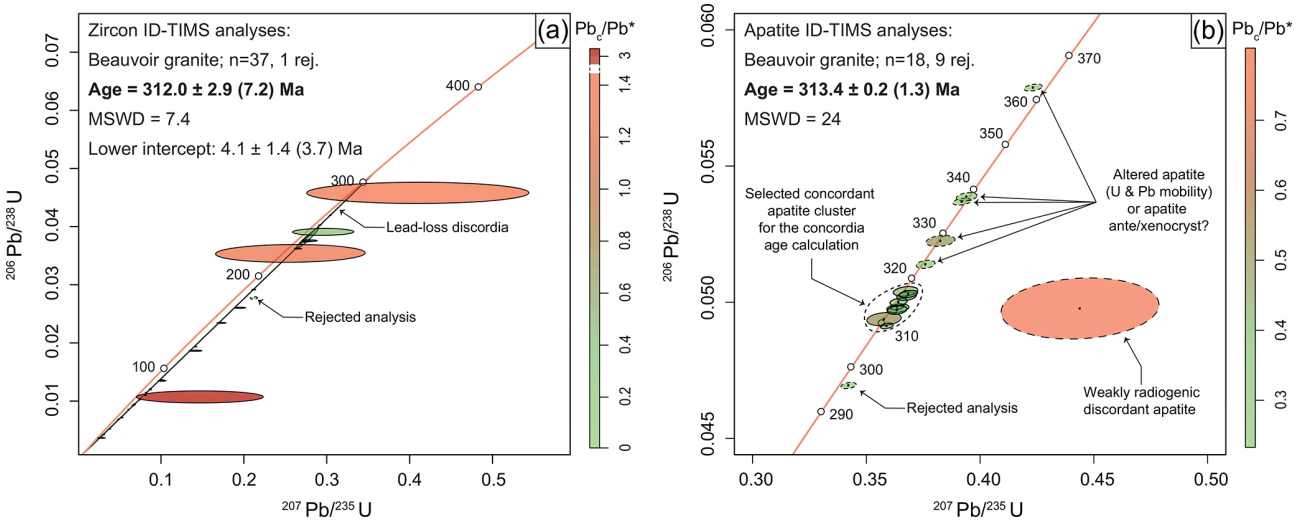

Figure 8. **(a)** Wetherill diagram showing the zircon analyses straddling a discordia line which intercepts the concordia at 312.0±2.9 (7.2) Ma (2σ). **(b)** Concordia Wetherill diagram showing the apatite analyses, corrected for the initial Pb (Pb isotopic composition at 300 Ma; Stacey and Kramers, 1975). The concordant apatite cluster between 309 and 318 Ma gives an age at 313.4 ± 0.2 (1.3) Ma (2σ). Coloured ellipses represent the ratio of common to radiogenic lead (Pb_c/Pb^*) of each zircon and apatite analysis. The higher this ratio is, the higher the analysis uncertainty is. Complete isotopic results can be found in the Supplement (Table S1).

by a zircon and its amorphous fraction published by Nasdala et al. (2001).

5.1.2 Zone 2: a hydrothermal origin

Zone 2 is represented by a continuous and interconnected matrix in which fragments of Zone 1 are embedded. The Zone 2 *T* site is notably enriched in Al and P cations (0.05 and 0.11 apfu; Table 1), whereas the *A* site is characterised by elevated Ca and U cations (0.06 and 0.03 apfu; Table 1). This Si deficiency in the Zone 2 *T* site is partially linked to the berlinite substitution: $2\,Si^{4+} \leftrightarrow P^{5+} + Al^{3+}$. The leftover P is incorporated into the zircon structure via the brabantite substitution, $2\,Si^{4+} + 2\,Zr^{4+} \leftrightarrow Ca^{2+} + (U^{4+}) + 2\,P^{5+}$, which also explains the Zr deficiency in the Zone 2 *A* site. If the incorporation of Al and P in Zone 2 zircon is fully explained by the berlinite and berlinite/brabantite substitutions, excess Ca must have been incorporated into Zone 2 in another way. U incorporation into zircon can only be partly explained by the coffinite substitution as zircon data plot below the 1 : 1 substitution vector (Fig. 4g). As with Ca, additional U eventually entered the zircon crystal lattice through the brabantite substitution. Incorporation of low-field-strength cations (e.g. Fe and Mn) in zircon structure is more complex to assess. Considering only the valence on these cations, they could substitute Zr in the eightfold site (*A* site) via the coupled substitution $Zr^{4+} \leftrightarrow 2\,(Mn^{2+} + Fe^{2+})$ (Fig. 4h). However, such substitution seems to be impossible considering the $Zr^{[8]}$ ionic radii (0.84 Å; Shannon, 1976) and those of $Mn^{2+[8]}$ and $Fe^{2+[8]}$ (0.96 and 0.92, respectively; Shannon, 1976). From their study on similar zircons, Pérez-Soba et al. (2014) proposed that $Fe^{2+[4]}$ together with $O^{2-[4]}$ could enter the four-coordinated interstitial (1.84 Å; Finch et al., 2001) site as the sum of their ionic radii is 2.01 Å (Shannon, 1976). Mn could substitute Zr in the zircon *A* site as also proposed by Pérez-Soba et al. (2014). Fluorine is likely localised in the zircon *T* site as F negatively correlates with Si (Fig. 4e), potentially involving a substitution $(SiO_4)^{4-} \leftrightarrow (F_4)^{4-}$. This fluorine incorporation in the zircon *T* site was already experimentally identified by Caruba et al. (1985), who synthesised hydrous zircon with up to 0.8 $(OH,F)_4$ apfu substituting the SiO_4 group. Another way to incorporate anions (i.e. OH^-, F^- and Cl^-) in zircon structure has for instance been proposed by Courtney-Davies (2019) in their study on metasomatic zircon in gold–copper granite deposits, where O^{2-} would be substituted by 2 (OH^-, Cl^-). In addition, it should be noted that the substitutions that experienced these zircons have a "snowball effect". Indeed, the first substitution of P + Al in the *T* site strongly disordered the early formed zircon crystal structure. This lattice was eventually more disordered after the Ca and U incorporation in the *A* site. Thus, it is also highly possible that other substituting elements (e.g. the Ca excess, water or other trace elements) entered the highly disordered zircon lattice in interstitial position apart from the main lattice sites (e.g. Finch et al., 2001; Breiter and Škoda, 2012).

Caruba et al. (1985) also noticed that the ν_3 (SiO_4) peak position of hydrous zircon is shifted to higher wavelengths when compared to pure zircon (1020 to 1045 cm^{-1}). On the other hand, the protracted α decay and zircon lattice damage leading to a metamict state are associated with an overall decrease in Raman band intensity as well as a shift towards lower wavenumbers (e.g. Nasdala et al., 2001, and Fig. 7c).

Thus, although Zone 2 corresponds to metamict zircon, the fact that its ν_3 (SiO_4) peak position is not that different from the one characterising Zone 1 (Fig. 7a) could be explained by the presence of water in the aperiodic Zone 2 structure. However, a spectroscopic analysis (e.g. Raman) on a complete aperiodic mineral should, by definition, lead to a flat spectrum (i.e. without peak), which is not what we observe in Zone 2 Raman spectra (Figs. 6g–i and 7a–c). A potential alternative would be that the apparent ν_3 (SiO_4) peak between 990 and 996 cm^{-1} is actually related not only to the SiO_4 tetrahedra vibrations but also to the PO_4 tetrahedra vibration. Indeed, considering the important phosphorus concentration in Zone 2 zircon and the fact that the A_{1g} (PO_4) vibrational band typically ranges between 985 and 1000 cm^{-1} (e.g. Švecová et al., 2016), it is likely that the observed peak in Zone 2 spectra can account for both SiO_4 and PO_4 tetrahedra vibrations.

The textures and chemical composition of Zone 2 raise the question of its origin (i.e. magmatic and/or hydrothermal). The incorporation of Al and P in the zircon T site was proposed by Breiter et al. (2006) to be a primary magmatic feature reflecting zircon crystallisation from an Al- and P-rich melt. A fully magmatic origin would imply that Zone 2 zircon crystallised from a compositionally different melt (or under very different physical conditions) than that from which Zone 1 crystallised. Such a melt would have to be strongly enriched in U, P, Al, F, Ca, Fe and Mn compared to the parental melt of Zone 1. Although extreme magmatic differentiation of the Beauvoir magmas has led to the formation of P-, Al- and F-rich residual liquids, this differentiation also induced melt depletion in Fe, Mn and Ca (Esteves et al., 2024a). Since Fe, Mn and Ca are positively correlated with P and F in Zone 2, these compositional variations cannot be linked to melt differentiation. Moreover, extreme fractionation would also have led to the formation of Hf-rich residual melt (Linnen and Keppler, 2002; Zaraisky et al., 2008; Wang et al., 2010). This is not recorded by Zone 2 zircon, which is on average less enriched in Hf compared to Zone 1 zircon (Fig. 4d). Thus, a magmatic origin for Zone 2 is inconsistent with the observed concentrations, and other processes were likely at stake. It is well documented that the Beauvoir rare-metal magmas experienced numerous stages of fluid exsolution prior to their complete solidification ($\sim$ 560 °C; Pichavant, 2022), as numerous fluid and brine inclusions mainly in quartz and topaz have been reported throughout the granite (Aïssa et al., 1987; Fouillac et al., 1987; Harlaux et al., 2017; Rocher et al., 2024). Based on a fluid inclusion study, Harlaux et al. (2017) showed that a first generation of exsolved brines (L1: 17 wt %–28 wt % NaCl eq.) from the Beauvoir silicate magma (i.e. deuteric fluids) occurred during magma crystallisation (from > 600 to 500 °C). This first generation is enriched in Na, Li, K, Al, Mn, Fe and F compared to the Beauvoir magmas (Aïssa et al., 1987; Harlaux et al., 2017). As hydrothermal apatite also precipitated from these fluids (Rocher et al., 2024), they were also eventually enriched in Ca and P. A second brine generation (L2: 32 wt %–48 wt % NaCl eq.) circulated below the Beauvoir solidus (520–400 °C; Aïssa et al., 1987). The mixing of these L2 fluids with meteoric fluids has formed a third fluid generation (L3: 2 wt %–5 wt % NaCl eq.) at 420–330 °C (Fouillac et al., 1987; Harlaux et al., 2017). From the dating of hydrothermal apatite, Rocher et al. (2024) showed that late and low-temperature (< 250 °C) hydrothermal fluids circulated throughout the Beauvoir granite at 268.3 ± 20.4 and 148.5 ± 26.6 Ma. Based on zircon leaching experiments, Geisler et al. (2002) demonstrated the capacity of low-temperature (175 °C during 1340 h) chloride-bearing fluids to leach metamict zircon containing an amorphous fraction of 85 % ($\sim 0.59.10^{16}\alpha$ decays mg^{-1}, which is slightly more than half of the actual Zone 1 zircon). Such interaction efficiently removed the Si^{4+} and Zr^{4+} cations from metamict zircon with subsequent replacement by Al^{3+} and Ca^{2+}. Such replacement processes are a common feature in zircons in highly differentiated systems that have experienced hydrothermal alteration (e.g. Černý and Siivola, 1980; Uher and Černý, 1998; Geisler et al., 2002, 2007; Van Lichtervelde et al., 2009; Breiter and Škoda, 2012; Troch et al., 2018; Courtney-Davies et al., 2019; Han et al., 2023; Jia et al., 2024). Therefore, the continuous compositional trends between Zones 1 and 2 (Fig. 4a–i) could potentially be explained by various replacement degrees of Zone 1 by Zone 2 material through reactions (i.e. dissolution–reprecipitation) with reactive fluids. The timing of these replacements and the nature of the involved fluids are discussed in the following section.

Two distinct scenarios could explain the replacement of Zone 1 by Zone 2 zircon: a replacement by late and low-temperature reactive fluids or by reactive, early and high-temperature fluids (i.e. deuteric and hydrothermal fluids). During the hydrothermal fluid circulations that occurred at $\sim$ 268 and $\sim$ 148 Ma (Rocher et al., 2024), Zone 1 zircon would have experienced $\sim 1.2 \times 10^{15}$ and $\sim 4.5 \times 10^{15}\alpha$ decays mg^{-1}, respectively, corresponding to an amorphous fraction of $\sim$ 5 % and $\sim$ 40 % (Nasdala et al., 2001). This Zone 1 damaged nature could have enhanced its replacement by low-temperature fluids to form Zone 2 zircon (e.g. Geisler et al., 2002, 2003a, b, 2007; Hoskin, 2005; Popov et al., 2024). However, such replacements (notably involving U) are known to reset, partially or totally, the zircon U-Pb system (Nasdala et al., 1998; Mezger and Krogstad, 1997; Geisler et al., 2003a, b; Popov et al., 2024). As the U-Pb system of Beauvoir zircon has not been reset at $\sim$ 268 or $\sim$ 148 Ma (single discordia line in Fig. 8a), it is unlikely that Zone 2 zircon formed during these late and low-temperature hydrothermal events. The formation of Zone 2-like zircon has also been attributed to zircon alteration under reactive deuteric fluids (Troch et al., 2018; Courtney-Davies et al., 2019; Han et al., 2023; Jia et al., 2024; Monnier et al., 2025). As such deuteric fluids started to circulate at the magmatic–hydrothermal transition, these fluids had to be able to dis-

solve pristine zircon grains, given the time required for α-decay-damaged zircon to form. As shown by the zircon in Fig. 3c, some continuous Zone 1 growth zones have not been replaced (e.g. the one containing cracks). This feature indicates that the original zircon (i.e. before its partial replacement) composed of Zone 1 material was not homogeneous (Fig. 9a), and some growth zones were more prone than others to being replaced (e.g. Černý and Siivola, 1980; Geisler et al., 2007; Van Lichtervelde et al., 2009). Such differences in the original zircon likely correspond to compositional variations that are directly linked to lattice ordering (Finch et al., 2001; Geisler et al., 2006) and so, to the resistance against reactive fluids (Černý and Siivola, 1980; Geisler et al., 2007). Indeed, in their study on high-U zircon that crystallised from the Chernobyl "lavas", Geisler et al. (2006) showed that high uranium incorporation in zircon is the source of microscopic strain within the zircon crystal structure. This strain is directly related to the size of U^{4+}, which is $\sim 16\,\%$ larger than Zr^{4+} (Shannon, 1976). A similar conclusion was drawn by Finch et al. (2001), who observed that xenotime substitution in zircon ($Zr^{4+} + Si^{4+} \leftrightarrow REE^{3+} + P^{5+}$) is associated with an increase in lattice strain. Thus, primary enriched (e.g. U- and/or trace element-rich) Zone 1 would have started to be preferentially dissolved and replaced at the magmatic–hydrothermal transition due to its more disordered crystal structure. The growth zones that are poorer in U and/or in trace elements, like the one in Fig. 9a, resisted these deuteric fluids and acted as a shield for zircon cores (e.g. Fig. 3c). Phosphorus-rich fractures that are contained in these growth zones likely indicate that these fluids entered zircon cores by fracturing these growth zones (Fig. 3a–e; Geisler et al., 2002). As these fractures are also connected to muscovite and quartz inclusions (Fig. 3d), it is most likely that these hydrothermal minerals that are common in Beauvoir greisen (Monnier et al., 2022; Cathelineau and Kahou, 2024; Rocher et al., 2024) crystallised at the same time as Zone 2 was formed (Fig. 9c).

Based on the compositional analyses of the Beauvoir L1 fluid inclusions (LA-ICP MS; Harlaux et al., 2017), hydrothermal fluids were 10 to 100 times more enriched in Fe and Mn than the Beauvoir silicate magmas. The elevated incorporation of Fe and Mn cations in Zone 2 would be related to these Fe- and Mn-rich fluids, a process also identified in other metasomatic zircon by Courtney-Davies et al. (2019). An external source of Fe^{2+} and Mn^{2+} via the meteoritic water influx is possible as well, as they partially leached the host micaschist before interacting with the Beauvoir magmas (Charoy et al., 2003; Harlaux et al., 2017; Rocher et al., 2024). Although P, Al, Ca and F concentrations in the Beauvoir fluid inclusions are unknown, the ubiquitous presence of hydrothermal apatite, topaz and fluorite in Beauvoir greisens (Monnier et al., 2020; Rocher et al., 2024) supports the high P, Al, Ca and F concentrations in these hydrothermal fluids. Part of this Ca could derive either from the alteration of magmatic plagioclase or from the leaching of the host micaschist (Charoy et al., 2003). The leaching of uranium-bearing oxides is often considered to explain the U-rich nature of hydrothermal fluids in leucogranites (e.g. Dolníček et al., 2014; Ballouard et al., 2017; Rocher et al., 2024). In the Beauvoir granite, U could have been either derived from the breakdown of magmatic pyrochlore as it experienced a significant U^{4+} removal during the Beauvoir magmatic–hydrothermal transition (Ohnenstetter and Piantone, 1988) or derived from the leaching of early formed uraninite (Cuney and Brouand, 1987).

Therefore, we propose that the formation of Zone 2 was progressively achieved through strain-controlled replacements (dissolution–reprecipitation) of Zone 1 under reactive deuteric fluids (Fig. 9b) and subsequent hydrothermal fluids (Fig. 9c) during the Beauvoir hydrothermal activity. As such, specific Zone 1 growth zones that were originally U- and/or trace element-rich were preferentially replaced (compared to the remaining and unreplaced Zone 1; Fig. 9a, b) due to their more disordered crystal structure. These replacements that started at the Beauvoir magmatic–hydrothermal transition ceased once the hydrothermal activity ended (or when these fluids were not reactive anymore relative to zircon grains; Fig. 9d). Then, the radionuclides (mostly U) contained in Beauvoir zircon progressively damaged Zones 1 and 2 due to their prolonged disintegration, leading to an almost amorphous Zone 1 and a completely amorphous Zone 2 (Fig. 9d). Additional elements might have migrated into and out of these amorphous and metamict zircon grains since at least 300 Ma (Fig. 9d) as element diffusivity in amorphous material is enhanced relative to that in pristine material (e.g. Cherniak et al., 1991; Geisler et al., 2003c, 2007). Consequently, the complex composition of Beauvoir zircon is a combination of its alteration by deuteric/hydrothermal fluids and by progressive element incorporation in relation to its protracted amorphisation.

5.1.3 Origin of Zr-5

The zircon grain Zr-5 is texturally different from the other Beauvoir zircon grains in that it does not present isolated Zone 1 within interconnected Zone 2 material (Fig. 10a). The Zr-5 core is characterised by a Si-rich zircon (Fig. 10b) containing numerous uraninite micro-inclusions (Fig. 10a, c). The distribution of these inclusions is not homogeneous as they are absent in the P-rich domain (Fig. 10d). On the other hand, the Zr-5 rim, which does not contain uraninite inclusion, is zoned with a progressive decrease in its U content (from ~ 5.5 wt % to 1 wt % UO_2; Fig. 10c) towards the crystal rim. These U variations are not associated with Si or P variations (Fig. 10b–d), suggesting that U was not incorporated through a brabantite substitution. On the other hand, U in Zr-5 is negatively correlated with Zr, which supports a U incorporation via the coffinite substitution (Fig. 4g). Although the Zr-5 data do not strictly fall on the $Zr^{4+} \leftrightarrow U^{4+}$ substitution vector, they are parallel to this vector at a lower

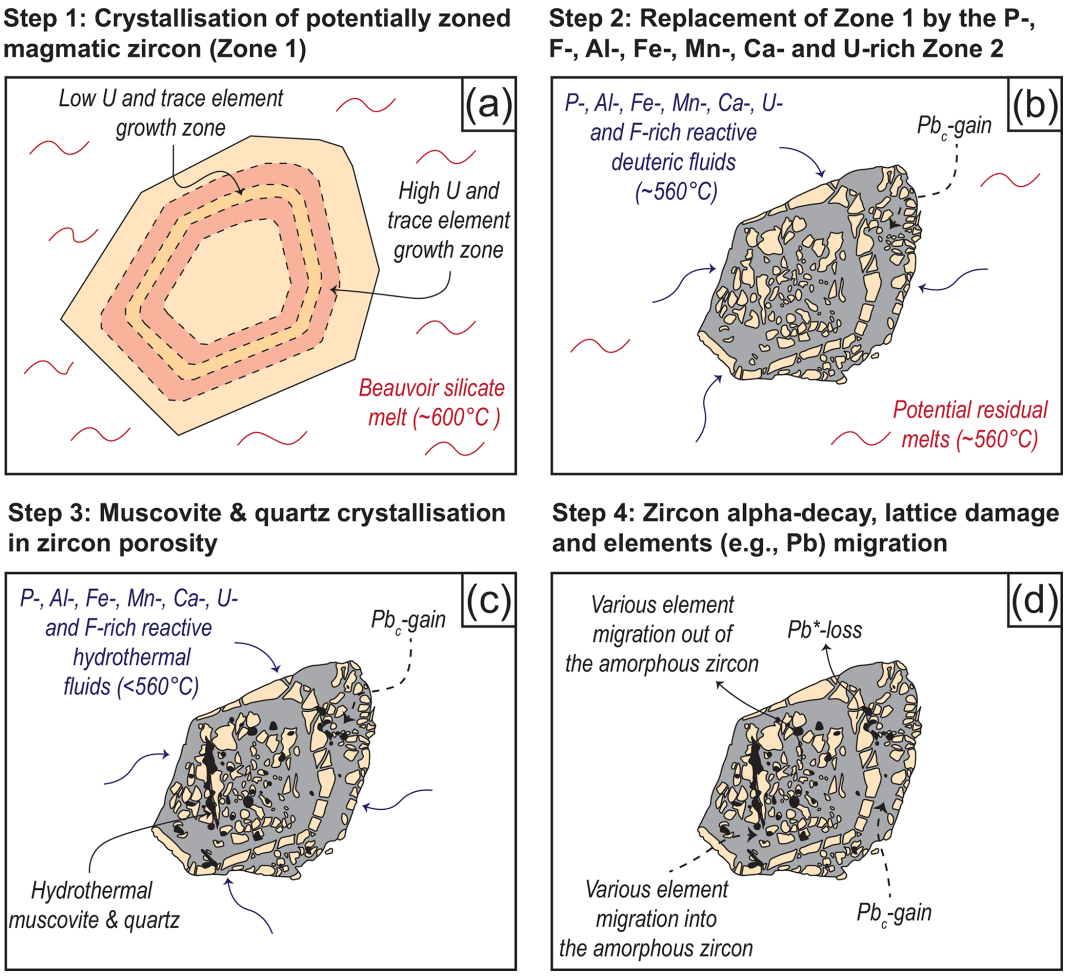

Figure 9. Schematic drawing of the formation of Beauvoir zircons. **(a)** Crystallisation of Zone 1 zircon from the Beauvoir silicate melt. Variations in melt composition through its differentiation formed compositionally distinct growth zones (notably in Hf and U). **(b)** Partial replacement (dissolution–reprecipitation) of Zone 1 by reactive deuteric fluids during the magmatic–hydrothermal transition forming Zone 2 zircon. U-rich Zone 1 growth zones were preferentially replaced due to their disordered crystal lattice, while U-poor Zone 1 growth zones were fractured. **(c)** Continuous Zone 1 replacement and crystallisation of hydrothermal muscovite and quartz in the zircon voids from reactive hydrothermal fluids. **(d)** End of the reactive hydrothermal circulation. The progressive alpha decay and lattice damage of Beauvoir zircon resulting in a metamict state is accompanied by element migration into and out of the zircon, including Pb* loss and Pb_c gain.

Zr value (Fig. 4g), reflecting another substitution involving Zr such as the hafnon substitution as Zr-5 contains ∼ 3 wt % HfO_2 (Fig. 4f). Although Zr-5 zircon is unique, its outer rim is compositionally similar to Zone 1 (Fig. 4e–i). Some local domains are enriched in P and depleted in Si (Fig. 10b, d), which eventually reflect the berlinite and brabantite substitution (Fig. 4a–d) during episodes of zircon alteration under reactive fluids. These Zr-5 alteration episodes were however much more limited than for the other zircon grains presenting the interconnected Zone 2 material. Thus, Zr-5 likely represents a Beauvoir zircon that has not undergone intense alteration by reactive fluids. An early zircon crystallisation stage would have formed U-rich zircon, while magmatic differentiation triggered U melt depletion, as evidenced by the U-poor nature of Zr-5 rims (Fig. 10c). Following this protracted magma crystallisation, Zr-5 experienced limited alteration from reactive fluids (Fig. 10f), leading to the formation of phosphorus-rich regions in replacement of the original Zr-5.

The origin of the uraninite inclusions in Zr-5 is more difficult to assess. Three main hypotheses could explain the presence of these inclusions: a contemporaneous uraninite growth with the zircon, uraninite precipitation during zircon dissolution–reprecipitation under reactive fluids (e.g. Geisler et al., 2007; Troch et al., 2018) or secondary exsolution. Although subhedral uraninite is present in the Beauvoir granite (Cuney and Autran, 1988), the fact that it is absent from all other studied zircons suggests that co-crystallisation prior to its entrapment is highly unlikely. Moreover, most inclusions have sigmoidal shape (Fig. 10a), in disagreement with the ex-

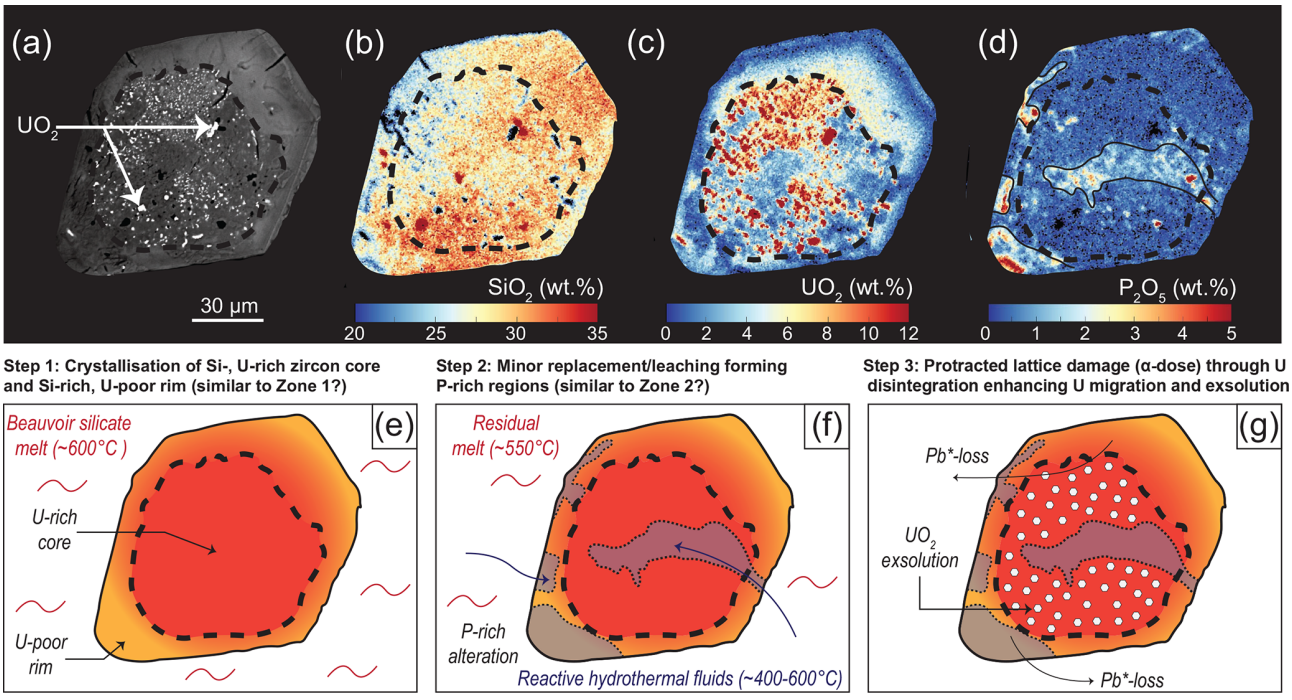

Figure 10. **(a)** BSE image of Zr-5. **(b)** SiO_2, **(c)** UO_2 and **(d)** P_2O_5 quantitative chemical maps of the same crystal in **(a)**. Note the sharp boundary between the crystal core, enriched in uraninite (UO_2) micro-inclusions, and the U-rich rim without inclusions, indicated by the dashed circle. Also note the spatial distribution pattern of muscovite and quartz inclusions that are spatially separated from the uraninite inclusions. **(e, f, g)** Schematic drawing of the formation of Zr-5. **(e)** Crystallisation of Zr-5 from the Beauvoir silicate melt. Uranium is progressively depleted in the melt leading to a UO_2 content decrease from core to rim. **(f)** Minor replacement and leaching of Zr-5 by reactive residual melt and reactive hydrothermal fluids forming phosphorus-rich domains at the expense of the early crystallised magmatic Zr-5. **(g)** Protracted Zr-5 α dose and lattice damage enhancing UO_2 exsolution via U migration through the amorphous zircon.

pected cubic shape if uraninite had crystallised from a melt. The presence of such inclusions in spongy zircon has also been proposed to be linked with dissolution–reprecipitation processes with hydrothermal fluids (e.g. Hetherington and Harlov, 2008, in xenotime and Troch et al., 2018, and Monnier et al., 2025, in zircon). For instance, the presence of rounded U-rich thorite, yttrialite and uraninite inclusions in metamict and spongy zircon from Yellowstone rhyolites was attributed by Troch et al. (2018) to (1) the dissolution of metastable U- and Th-rich zircon and (2) the simultaneous reprecipitation of these inclusions with a stable U- and Th-poorer zircon. Although we showed that Beauvoir zircon grains were replaced by reactive fluids forming Zone 2 zircon (Fig. 9b), these Zone 2 domains do not contain these uraninite micro-inclusions. In addition, as the P-rich, altered parts of Zr-5 are those that do not contain these uraninite micro-inclusions (Fig. 10a, d), it is unlikely that these inclusions are associated with dissolution–reprecipitation processes. We therefore favour the third hypothesis, whereby uraninite formed by exsolution from a U-rich core, corresponding to the early U-rich Zr-5 crystallisation (Fig. 10e). Since Zr^{4+} is $\sim 16\,\%$ smaller than U^{4+} (Shannon, 1976), the coffinite substitution is not ideal, and a miscibility gap exists between coffinite and zircon end-members (Ferriss et al., 2010). Based on solubility experiments, Ushakov et al. (1999) determined that the maximum $USiO_4$ solubility in zircon is less than 6 % mol. at 1400–1500 °C, corresponding to a concentration of ~ 8.9 wt % UO_2. This maximum solubility is likely to decrease at lower crustal temperatures (< 500 °C). This lack of exsolution texture in zircon might be the result of slow U^{4+} diffusion in zircon (6.8×10^{-29} m^2 s^{-1} at 1100 °C; Cherniak et al., 1997), and therefore, U-rich zircons (> 9 wt % UO_2) would correspond to metastable crystals (Geisler et al., 2007; Ferriss et al., 2010; Troch et al., 2018). However, it has been shown that the elemental diffusivity in metamict zircon, in which a significant part of the crystal is amorphous and material-depleted, is significantly faster than in a crystalline zircon (Cherniak et al., 1991; Geisler et al., 2003c, 2007). Thus, it seems possible that uranium mobility in amorphous material would ideally create sites of exsolved U-bearing phases (uraninite or coffinite). Following this, the Zr-5 uraninite micro-inclusions (Fig. 10a) would have been formed via a U exsolution promoted by the intense amorphisation of the Zr-5 crystal structure (Fig. 10g). Thus, the sharp boundary between the Zr-5 core and its rim (Fig. 10a–g) would potentially reflect the U concentration threshold at which U exsolution occurred in Beauvoir zircon grains (~ 6 wt % UO_2; Fig. 10c). The ab-

sence of these UO_2 exsolutions in the P-rich and replaced Zr-5 core would thus be linked to dissolution–reprecipitation processes (e.g. Troch et al., 2018) where U-poorer zircon would have replaced the originally U-rich zircon. Using simple image processing, the Zr-5 core is composed of ∼ 11 % exsolved uraninite and ∼ 89 % zircon. Considering a concentration of 100 wt % UO_2 in uraninite and 6 wt % UO_2 in zircon, the original composition of the Zr-5 core after crystallisation would be ∼ 16.3 wt % UO_2. Such a concentration is far above that in Beauvoir Zone 1 zircons, thus indicating that the Zr-5 core does not correspond to Zone 1 and must have crystallised earlier as U behaves compatibly in such evolved magmas (Friedrich et al., 1987). On the contrary, the Zr-5 rim could correspond to the preserved Zone 1 zircon.

5.2 Beauvoir geochronology

5.2.1 Zircon lattice damage inducing lead loss

All but one of the Beauvoir analysed zircons form a discordia line, whose upper intercept represents their crystallisation age (Fig. 8a). The fact that the origin of the discordia is anchored at the origin of the Wetherill plot (Fig. 8a) indicates that these zircons have experienced continuous lead loss since their crystallisation as a result of their metamict lattice state (Mezger and Krogstad, 1997; Fig. 9b–d). Therefore, no effect of the late Permian and Jurassic hydrothermal circulations, which have been identified in Beauvoir apatite (Rocher et al., 2024), is identified here. As mentioned above, Zones 1 and 2 are highly damaged due to their high uranium concentration. Based on molecular-dynamics simulations, Geisler et al. (2003c) showed that the accumulation of radiation damage can form interconnected regions of amorphous and depleted matter, which promotes element diffusivity through these depleted regions. Two main thresholds have been identified during a progressive zircon amorphisation (Salje et al., 1999; Geisler et al., 2003c). The first threshold is reached when the amorphous domains are interconnected (∼ 30 % of amorphous domains). The second threshold, corresponding to a higher degree of amorphisation (∼ 70 %), is reached when the crystalline materials are no longer connected and form isolated crystalline islands in an amorphous environment. In order to quantify when these thresholds were reached for Zones 1 and 2, we calculated the number of α decays mg^{-1} that these zircons have undergone since their crystallisation (Fig. 11a). To do so, the initial U concentration of Zones 1 and 2 has been calculated based on its averaged present-day U concentration (Table 1). The progressive α-decay events experienced by Zones 1 and 2 were then modelled based on the U radioactive decay of Jaffey et al. (1971). Although simplistic, these models eventually simulate, in the first order, the evolution of the crystal structure of Zones 1 and 2 through time (see Table S1 in the Supplement). At $t = 0$ (i.e. ∼ 313 Myr ago), radionuclide decay had just started, and thus, their structure was fully crystalline (Fig. 11a–b). The first threshold was reached after ∼ 150 Ma for Zone 1, whereas it was attained after ∼ 45 Ma for Zone 2 (Fig. 11a). Such a difference is easily explained by their different U concentrations (Table 1). The second threshold, corresponding to isolated crystalline zircon within an amorphous material, was reached after 285 Ma for Zone 1 and after 80 Ma for Zone 2 (Fig. 11a). At this point, most of the crystal is amorphous, further enhancing the processes of elemental mobility and lead loss. Such results imply that analysed Beauvoir zircons that are composed predominantly of Zone 2 material eventually experienced more radiogenic lead loss than those composed predominantly of Zone 1 material. These proportional differences would therefore be at the origin of variations in the degree of discordance of the Beauvoir zircons (Fig. 8a).

5.2.2 The apatite record and other dating methods

Concordant apatite ages spread from 362.7 ± 0.6 to 295.7 ± 0.6 Ma (Fig. 8b), potentially indicating that various apatite populations crystallised during different magmatic episodes. The main apatite population has $^{206}Pb/^{238}U$ ages ranging from 309.2 ± 0.5 to 317.0 ± 0.9 Ma with a concordant age of 313.4 ± 0.2 (1.3) Ma, which likely corresponds to the Beauvoir crystallisation age. This age is similar to the one obtained with a larger uncertainty by Rocher et al. (2024) on magmatic apatite (Apatite I) at 314.6 ± 4.7 Ma, which is also within the uncertainty of our ages from Beauvoir zircon – 312.0 ± 2.9 (7.2) Ma – and that obtained by Melleton et al. (2015) at 317 ± 6 Ma (U-Pb, columbite–tantalite). However, this apatite age is significantly younger than the zircon age reported from Beauvoir microgranite ($Zr_{\mu G}$: 323 ± 4 Ma – U-Pb, LA-ICP MS; Monnier, 2018) and, conversely, significantly older than the age obtained on Beauvoir lepidolite (308 ± 2 Ma – Ar–Ar; Cheilletz et al., 1992). Four older concordant apatite grains have crystallisation ages of 323.0±0.7, 328 ± 1, 337.1 ± 0.6 and 362.7 ± 0.6 Ma (Fig. 8b) and could correspond either to an artefact linked to U mobility in these apatite crystals (Popov et al., 2024) or to apatite antecrysts/xenocrysts (e.g. Popov et al., 2020; Barrie Clarke et al., 2023). Although bluish (i.e. magmatic) apatite grains were carefully handpicked, older apparent ages could be the result of U mobility in the presence of hydrothermal fluids. Moreover, it has been shown that thermally activated volume diffusion of Pb in apatite can locally create domains that are apparently older than formation ages if U is zoned (Paul et al., 2019; Popov and Spikings, 2021).

Therefore, as we may have analysed fragments of apatite (i.e. due to the rock fragmentation) combined with the intense hydrothermal activity that occurred at Beauvoir, it may well be that U mobility between these apparent old apatite grains and fluids is at the origin of these older dates, making them geologically meaningless (Popov et al., 2024). In addition, such partial opening of these apatite U-Pb isotopic systems would thus be at the origin of the scatter ob-

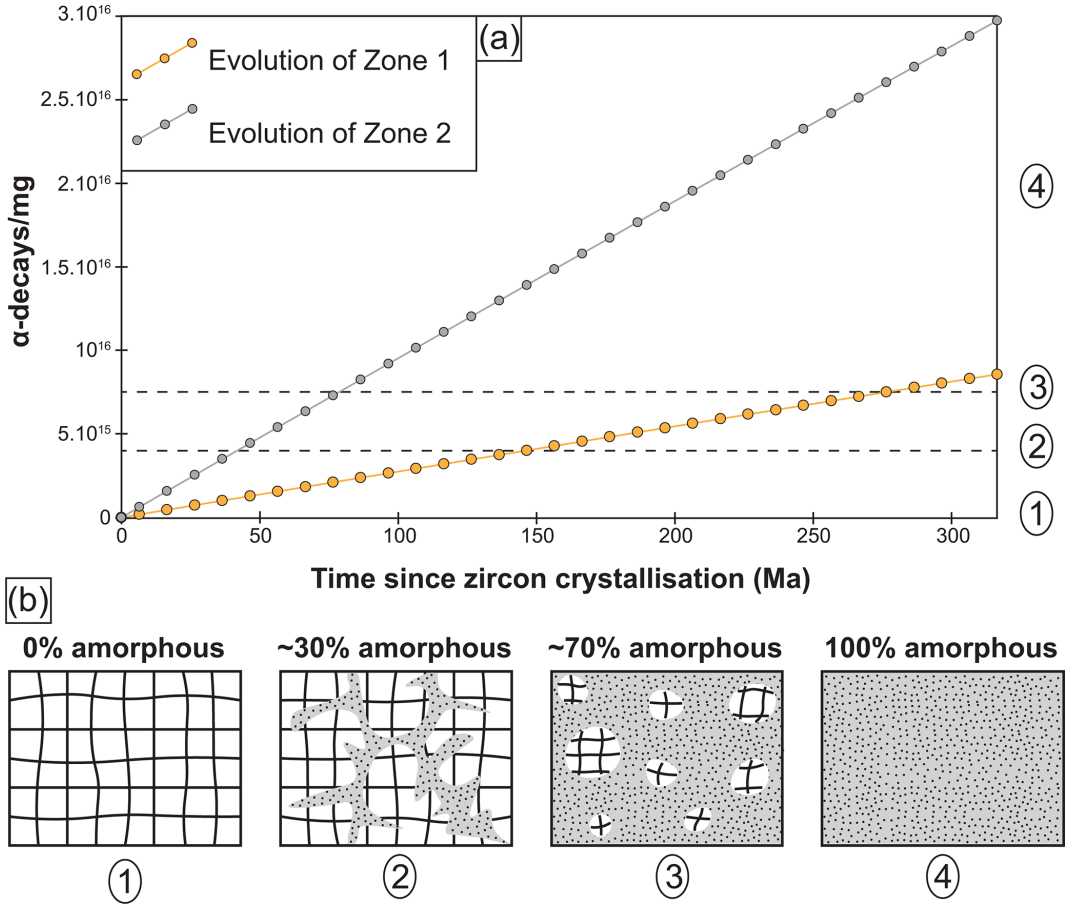

Figure 11. **(a)** Theoretical evolution of the number of α decays mg^{-1} experienced by Zones 1 and 2 for 313.4 Ma. **(b)** Schematic representation of the four different steps characterising zircon structure during their protracted lattice damage through radionuclide disintegration, adapted from Murakami et al. (1991). The estimation of the amorphous degree for each is from Geisler et al. (2007), and their relations with the number of α doses that experienced zircon are from Nasdala et al. (2001). See text for explanations on the significance of the four different steps.

served in the Tera–Wasserburg space when compared with the selected concordant apatite population from which the Beauvoir crystallisation age has been determined (Supplement, Fig. S3). Nevertheless, we cannot conclude or exclude whether such U mobility in these older apatite grains actually occurred. Another explanation would be that the older apatite ages represent antecrysts and/or xenocrysts. Indeed, the early crystallisation of apatite in Beauvoir magmas, which is attested by their inclusion in early formed topaz (Rocher et al., 2024), indicates that Beauvoir melts were eventually saturated in phosphorus at the time of their intrusion into the Beauvoir reservoir. The uptake of apatite antecrysts and xenocrysts by such phosphorus-saturated melts during their ascent through the magmatic plumbery would thus theoretically prevent their dissolution (although it might slightly disturb their U-Pb system). As such, the 323.0 Ma apatite could have crystallised during the same magmatic episode as $Zr_{\mu G}$, while older apatite grains may be associated with previous magmatic events that occurred within the Sioule area such as the Pouzol-Servant magmatism at ca. 330 Ma (Pin, 1991) as well as with older gneisses belonging to the Upper Gneiss Unit (ca. 350–360 Ma; Do Couto et al., 2016). However, it is not possible to invoke a recycling process to account for the presence of the 296 Ma concordant apatite. Such apatite might have experienced localised late fluid circulation that reopened its isotopic system and may be associated with the late Permian hydrothermal fluid circulation event identified by Rocher et al. (2024) at 268.3 ± 20.4 Ma.

5.3 Implications for dating rare-metal granites

Although the use of U-Pb CA-ID-TIMS geochronology on zircons is so far the most accurate technique to constrain when and how long a plutonic assembly occurred (e.g. Schoene et al., 2012; Schaltegger et al., 2021), its use in highly differentiated systems such as rare-metal granites and pegmatites is limited due to the high uranium concentration of zircon, associated decay-related damage and ubiquitous

lead loss. Moreover, as highlighted by the present study, hydrothermal activity, which is common in such differentiated systems, strongly modifies original magmatic zircons and disturbs their isotopic signature. For a moderately damaged zircon grain without significant interaction with hydrothermal fluids, this issue can possibly be mitigated by chemical abrasion (e.g. McKanna et al., 2024; Schaltegger et al., 2024). For the strongly metamict zircons of the Beauvoir granite ($\sim 10^{16} \alpha$ doses mg^{-1}), the chemical abrasion step cannot discriminate between more and less damaged zircon domains because the entire grain is beyond the second threshold (> 70 % metamict domains; Fig. 11). Thus, the use of high-precision zircon geochronology (CA-ID-TIMS) in such strongly differentiated systems is highly limited and restricted to the upper-intercept calculation of a lead loss discordia (Fig. 8a).

On the other hand, since apatite is a common magmatic mineral in highly differentiated granites and pegmatites, and combined with its closure temperature, the application of apatite geochronology allows us to acquire the most accurate Beauvoir emplacement age so far at 313.4 ± 0.2 (1.3) Ma (Fig. 8b). For comparison, LA-ICP MS dating is associated with a higher uncertainty as illustrated with the ages obtained on the Beauvoir magmatic apatites, 314.6 ± 4.7 Ma (Rocher et al., 2024), and columbite–tantalites, 317 ± 6 Ma (Melleton et al., 2015). Further developments on high-precision ID-TIMS analyses of other U-bearing minerals such as cassiterite (e.g. Carr et al., 2020), wolframite (e.g. Romer and Lüders, 2006; Carr et al., 2021) or columbite–tantalite (e.g. Romer and Smeds, 1994; Yang et al., 2023) would likely increase our understanding of the emplacement and mineralisation processes related to highly differentiated rare-metal silicic melts.

6 Conclusions

Zircons from the Beauvoir rare-metal granite are mostly composed of two distinct materials: Zones 1 and 2. Zone 1, which is Si- and Zr-rich, directly crystallised from the Beauvoir silicate melt. The P-, Al-, F-, Ca-, Fe-, Mn- and U-rich Zone 2 zircon is attributed to partial replacement of Zone 1 by reactive deuteric fluids during the Beauvoir hydrothermal activity. This partial replacement process has led to isolated rounded Zone 1 material within the interconnected Zone 2 material. Once the circulation of these fluids stopped, it took ~ 105 and ~ 45 Ma for Zones 1 and 2, respectively, to reach the point where amorphous domains are interconnected, whereas the second threshold where crystalline islands were isolated inside a metamict (i.e. amorphous) matrix was reached after ~ 285 and ~ 80 Ma for Zones 1 and 2, respectively. As a result, the entire volume of any Beauvoir zircon is almost completely amorphous today. Another zircon population containing several uraninite micro-inclusions likely documents, for the first time, uraninite exsolution in uranium-rich zircon. This uraninite exsolution was likely triggered by the primary uranium-rich composition before becoming oversaturated during the cooling of the Beauvoir system. Uranium migration was then enhanced by the advanced degree of zircon lattice disordering, allowing U^{4+} migration through the amorphous zircon.

Although we used the most accurate method for zircon geochronology (CA-ID-TIMS), the Beauvoir zircons were too damaged (i.e. metamict) to survive the chemical abrasion step. Analyses of the total dissolutions have led to a well aligned discordia with an upper intercept of 312 ± 2.9 (7.2) Ma. This age, within the uncertainty of previous Beauvoir dating, might reflect the end of the Beauvoir main reactive magmatic–hydrothermal activity (before subsequent reactivation at Permian and/or Jurassic times; Rocher et al., 2024). The high degree of discordance is related to extensive radiogenic lead loss since the zircon crystallisation. This radiogenic lead (in addition to other elements) efficiently diffused through zircon grains via elemental diffusion through interconnected pathways in amorphous materials. Compared to zircon geochronology, apatite U-Pb ID-TIMS analyses yield a Beauvoir crystallisation age of 313.4 ± 0.2 (1.3) Ma, which is the most precise dating of the Beauvoir granite so far.

Thus, although zircon texture and chemical composition can provide significant insights into the magmatic–hydrothermal transition of highly differentiated systems such as rare-metal granites, their use to accurately date these systems is not the optimal approach. The combined primary U-rich nature inducing lattice damage and enhancing lead migration, together with the partial replacement during the magmatic–hydrothermal transition, strongly disturbs the original U-Pb isotopic signature. We thus envision that alternative high-precision ID-TIMS methods applied to other accessory minerals such as apatite would be more appropriate and appear to be a powerful tool for future studies aiming at obtaining a better understanding of the emplacement and mineralisation of such systems.

Data availability. All the data presented in this contribution are given in the Supplement. The zircon electron-probe micro-analysis (EPMA) and micro-Raman analyses, zircon inclusion analyses, and zircon–apatite U-Pb CA-ID-TIMS data can be obtained via https://doi.org/10.24396/ORDAR-155 (Esteves et al., 2024b).

Supplement. The supplement related to this article is available online at https://doi.org/10.5194/ejm-37-667-2025-supplement.

Author contributions. NE collected the samples, prepared them, carried out the U-Pb chemistry as well as EPMA and micro-Raman analyses, analysed the data, and wrote the first draft. PB, LF and US designed the research. MO and ANP assisted NE in U-Pb chemistry

and carried out the U-Pb analyses. All the authors participated in the elaboration of this contribution.

Competing interests. The contact author has declared that none of the authors has any competing interests.

Disclaimer. Publisher's note: Copernicus Publications remains neutral with regard to jurisdictional claims made in the text, published maps, institutional affiliations, or any other geographical representation in this paper. While Copernicus Publications makes every effort to include appropriate place names, the final responsibility lies with the authors.

Acknowledgements. The authors thank Jérémie Melleton (BRGM) for assistance during borehole sampling at BRGM as well as the Steval (GeoRessources) team for their assistance using the Selfrag instrument. Andreï Lecomte and Marie-Camille Caumon (GeoRessources) are warmly thanked for their help and assistance during electron-probe micro-analyses and micro-Raman measurements, respectively. NE thanks Christophe Ballouard and Simon Couzinié for the fruitful discussions related to the Beauvoir zircons. We are grateful for the constructive and helpful comments made by the two anonymous reviewers and to Martine Buatier and Sergey Krivovichev for the editorial handling. This is CRPG contribution no. 2879.

Financial support. This study has been supported by the French National Research Agency with the reference ANR-10-LABX-21-RESSOURCES21 grant and INSU/CNRS TelluS grant (2022), both given to PB. NE acknowledges a DrEAM grant from "Lorraine Université d'Excellence" for funding him in Geneva.

Review statement. This paper was edited by Martine Buatier and reviewed by two anonymous referees.

References

Abdalla, H. M., Helba, H., and Matsueda, H.: Chemistry of zircon in rare metal granitoids and associated rocks, Eastern Desert, Egypt, Resour. Geol., 59, 51–68, https://doi.org/10.1111/j.1751-3928.2008.00079.x, 2009.

Aïssa, M., Weisbrod, A., and Marignac, C.: Caractéristiques chimiques et thermodynamiques des circulations hydrothermales du site d'Echassières, Géologie Fr., 2–3, 335–350, 1987.

Alekseev, V. I., Polyakova, E. V., Machevariani, M. M., and Marin, Yu. B.: Evolution of zircons from postorogenic intrusive series with Li-F granites, Russian Far East, Geol. Ore Depos., 56, 513–530, https://doi.org/10.1134/S1075701514070034, 2014.

Aubert, G.: Les coupoles granitiques de Montebras et d'Echassières (Massif Central français) et la génèse de leurs mineralisations en étain, lithium, tungstène et béryllium, Mém. BRGM Orléans, 46, 349pp., 1969.

Ballouard, C., Poujol, M., Boulvais, P., Mercadier, J., Tartèse, R., Venneman, T., Deloule, E., Jolivet, M., Kéré, I., Cathelineau, M., and Cuney, M.: Magmatic and hydrothermal behavior of uranium in syntectonic leucogranites: The uranium mineralization associated with the Hercynian Guérande granite (Armorican Massif, France), Ore Geol. Rev., 80, 309–331, https://doi.org/10.1016/j.oregeorev.2016.06.034, 2017.

Barboni, M., Schoene, B., Ovtcharova, M., Bussy, F., Schaltegger, U., and Gerdes, A.: Timing of incremental pluton construction and magmatic activity in a back-arc setting revealed by ID-TIMS U/Pb and Hf isotopes on complex zircon grains, Chem. Geol., 342, 76–93, https://doi.org/10.1016/j.chemgeo.2012.12.011, 2013.

Barboni, M., Annen, C., and Schoene, B.: Evaluating the construction and evolution of upper crustal magma reservoirs with coupled U/Pb zircon geochronology and thermal modeling: A case study from the Mt. Capanne pluton (Elba, Italy), Earth Planet. Sc. Lett., 432, 436–448, https://doi.org/10.1016/j.epsl.2015.09.043, 2015.

Barrie Clarke, D., Harlov, D. E., Brenan, J. M., Jähkel, A., Cichy, S. B., Wilke, F. D., and Yang, X.: Assimilation of xenocrystic apatite in peraluminous granitic magmas, Am. Mineral., 108, 1421–1435, https://doi.org/10.2138/am-2022-8668, 2023.

Bowring, J. F., McLean, N. M., and Bowring, S. A.: Engineering cyber infrastructure for U-Pb geochronology: Tripoli and U-Pb_Redux, Geochem. Geophys. Geosyst., 12, 1–19, https://doi.org/10.1029/2010GC003479, 2011.

Breiter, K. and Škoda, R.: Vertical zonality of fractionated granite plutons reflected in zircon chemistry: the Cínovec A-type versus the Beauvoir S-type suite, Geol. Carpathica, 63, 383–398, https://doi.org/10.2478/v10096-012-0030-6, 2012.

Breiter, K., Förster, H.-J., and Škoda, R.: Extreme P-, Bi-, Nb-, Sc-, U- and F-rich zircon from fractionated perphosphorous granites: The peraluminous Podlesí granite system, Czech Republic, Lithos, 88, 15–34, https://doi.org/10.1016/j.lithos.2005.08.011, 2006.

Carr, P. A., Zink, S., Bennett, V. C., Norman, M. D., Amelin, Y., and Blevin, P. L.: A new method for U-Pb geochronology of cassiterite by ID-TIMS applied to the Mole Granite polymetallic system, eastern Australia, Chem. Geol., 539, 119539, https://doi.org/10.1016/j.chemgeo.2020.119539, 2020.

Carr, P. A., Mercadier, J., Harlaux, M., Romer, R. L., Moreira, E., Legros, H., Cuney, M., Marignac, C., Cauzid, J., Salsi, L., Lecomte, A., Rouer, O., and Peiffert, C.: U/Pb geochronology of wolframite by LA-ICP-MS; mineralogical constraints, analytical procedures, data interpretation, and comparison with ID-TIMS, Chem. Geol., 584, 120511, https://doi.org/10.1016/j.chemgeo.2021.120511, 2021.

Caruba, R., Baumer, A., Ganteaume, M., and Iacconi, P.: An experimental study of hydroxyl groups and water in synthetic and natural zircons: a model of the metamict state, Am. Mineral., 70, 1224–1231, 1985.

Cathelineau, M. and Kahou, Z. S.: Discrimination of Muscovitisation Processes Using a Modified Quartz–Feldspar Diagram: Application to Beauvoir Greisens, Minerals, 14, 746, https://doi.org/10.3390/min14080746, 2024.

Černý, P.: Geochemical and petrogenetic features of mineralization in rare-element granitic pegmatites in the

light of current research, Appl. Geochem., 7, 393–416, https://doi.org/10.1016/0883-2927(92)90002-K, 1992.

Černý, P. and Siivola, J.: The Tanco pegmatite at Bernic Lake, Manitoba. XII. Hafnian zircon, Can. Mineral., 18, 313–321, 1980.

Černý, P., Meintzer, R. E., and Anderson, A. J.: Extreme fractionation in rare-element granitic pegmatites; selected examples of data and mechanisms, Can. Mineral., 23, 381–421, 1985.

Charoy, B., Chaussidon, M., Le Carlier De Veslud, C., and Duthou, J.: Evidence of Sr mobility in and around the albite–lepidolite–topaz granite of Beauvoir (France): an in-situ ion and electron probe study of secondary Sr-rich phosphates, Contrib. Mineral. Petrol., 145, 673–690, https://doi.org/10.1007/s00410-003-0458-x, 2003.

Cheilletz, A., Archibald, D. A., Cuney, M., and Charoy, B.: Ages 40Ar/39Ar du leucogranite à topaze-lépidolit de Beauvoir et des pegmatites sodolithiques de Chédeville (Nord du Massif Central, France). Signification pétrologique et géodynamique., Comptes Rendus Académie Sci. Paris, 315, 329–336, 1992.

Chelle-Michou, C., Chiaradia, M., Ovtcharova, M., Ulianov, A., and Wotzlaw, J.-F.: Zircon petrochronology reveals the temporal link between porphyry systems and the magmatic evolution of their hidden plutonic roots (the Eocene Coroccohuayco deposit, Peru), Lithos, 198, 129–140, https://doi.org/10.1016/j.lithos.2014.03.017, 2014.

Cherniak, D. J., Lanford, W. A., and Ryerson, F.: Lead diffusion in apatite and zircon using ion implantation and Rutherford backscattering techniques, Geochim. Cosmochim. Ac., 55, 1663–1673, https://doi.org/10.1016/0016-7037(91)90137-T, 1991.

Cherniak, D. J., Hanchar, J. M., and Watson, E. B.: Diffusion of tetravalent cations in zircon, Contrib. Mineral. Petrol., 127, 383–390, https://doi.org/10.1007/s004100050287, 1997.

Claiborne, L., Miller, C. F., Walker, B. A., Wooden, J. L., Mazdab, F. K., and Bea, F.: Tracking magmatic processes through Zr/Hf ratios in rocks and Hf and Ti zoning in zircons: An example from the Spirit Mountain batholith, Nevada, Mineral. Mag., 70, 517–543, https://doi.org/10.1180/0026461067050348, 2006.

Condon, D. J., Schoene, B., McLean, N. M., Bowring, S. A., and Parrish, R. R.: Metrology and traceability of U–Pb isotope dilution geochronology (EARTHTIME Tracer Calibration Part I), Geochim. Cosmochim. Ac., 164, 464–480, https://doi.org/10.1016/j.gca.2015.05.026, 2015.

Courtney-Davies, L., Ciobanu, C. L., Verdugo-Ihl, M. R., Slattery, A., Cook, N. J., Dmitrijeva, M., Keyser, W., Wade, B. P., Domnick, U. I., Ehrig, K., Xu, J., and Kontonikas-Charos, A.: Zircon at the Nanoscale Records Metasomatic Processes Leading to Large Magmatic–Hydrothermal Ore Systems, Minerals, 9, 364, https://doi.org/10.3390/min9060364, 2019.

Cuney, M. and Autran, A.: Le forage scientifique d'Echassières (Allier). Une clé pour la compréhension des mécanismes magmatiques et hydrothermaux associés aux granites à métaux rares. Thème 8: évolution d'un apex granitique, Doc. BRGM, 124, BRGM, Orléans, France, 437 pp., 1988.

Cuney, M. and Brouand, M.: Minéralogie et géochimie de U et Th dans le granite de Beauvoir et les micaschistes encaissants, comparaison avec la géochimie de l'étain, Geol. Fr., 2–3, 247–257, 1987.

Cuney, M., Autran, A., and Burnol, L.: Programme Géologie profonde de la France. Troisième phase d'investigation: 1985–1986. Thème 8: Evolution géochimique et métallogénique d'un apex granitique (Echassières), Doc. BRGM, 100, BRGM, Orléans, France, 323 pp., 1985.

Cuney, M., Marignac, C., and Weisbrod, A.: The Beauvoir topaz-lepidolite albite granite (Massif Central, France); the disseminated magmatic Sn-Li-Ta-Nb-Be mineralization, Econ. Geol., 87, 1766–1794, https://doi.org/10.2113/gsecongeo.87.7.1766, 1992.

Dawson, P., Hargreave, M. M., and Wilkinson, G. R.: The vibrational spectrum of zircon ($ZrSiO_4$), J. Phys. C, 4, 240–256, https://doi.org/10.1088/0022-3719/4/2/014, 1971.

Do Couto, D., Faure, M., Augier, R., Cocherie, A., Rossi, P., Li, X.-H., and Lin, W.: Monazite U–Th–Pb EPMA and zircon U–Pb SIMS chronological constraints on the tectonic, metamorphic, and thermal events in the inner part of the Variscan orogen, example from the Sioule series, French Massif Central, Int. J. Earth Sci., 105, 557–579, https://doi.org/10.1007/s00531-015-1184-0, 2016.

Dolníček, Z., René, M., Hermannová, S., and Prochaska, W.: Origin of the Okrouhlá Radouò episyenite-hosted uranium deposit, Bohemian Massif, Czech Republic: fluid inclusion and stable isotope constraints, Miner. Deposita, 49, 409–425, https://doi.org/10.1007/s00126-013-0500-5, 2014.

Drabon, N., Kirkpatrick, H. M., Byerly, G. R., and Wooden, J. L.: Trace elements in zircon record changing magmatic processes and the multi-stage build-up of Archean protocontinental crust, Geochim. Cosmochim. Ac., 373, 136–150, https://doi.org/10.1016/j.gca.2024.03.014, 2024.

Esteves, N., Bouilhol, P., Cuney, M., and France, L.: Small pluton construction through sills stacking, amalgamation and differentiation: Insight from the Beauvoir granite (Massif Central, France), J. Petrol., submitted, https://doi.org/10.31223/X5KT5V, 2024a.

Esteves, N., Bouilhol, P., Schaltegger, U., Ovtcharova, M., Navin-Paul, A., and France, L.: Dataset related to the article "The magmatic-hydrothermal transition record in zircon: Implication on zircon texture, composition and rare-metal granite dating (Beauvoir granite, French Massif Central)", OTELO [data set], https://doi.org/10.24396/ORDAR-155, 2024b.

Farina, F., Weber, G., Hartung, E., Rubatto, D., Forni, F., Luisier, C., and Caricchi, L.: Magma flux variations triggering shallow-level emplacement of the Takidani pluton (Japan): Insights into the volcanic-plutonic connection, Earth Planet. Sc. Lett., 635, 118688, https://doi.org/10.1016/j.epsl.2024.118688, 2024.

Faure, M., Grolier, J., and Pons, J.: Extensional ductile tectonics on the Sioule metamorphic series (Variscan French Massif Central), Geol. Rundsch., 82, 461–474, https://doi.org/10.1007/BF00212410, 1993.

Faure, M., Lardeaux, J.-M., and Ledru, P.: A review of the pre-Permian geology of the Variscan French Massif Central, Comptes Rendus Geosci., 341, 202–213, https://doi.org/10.1016/j.crte.2008.12.001, 2009.

Ferriss, E. D. A., Ewing, R. C., and Becker, U.: Simulation of thermodynamic mixing properties of actinide-containing zircon solid solutions, Am. Mineral., 95, 229–241, https://doi.org/10.2138/am.2010.3318, 2010.

Finch, R. J., Hanchar, J. M., Hoskin, P. W. O., and Burns, P. C.: Rare-earth elements in synthetic zircon: Part 2. A single-crystal X-ray study of xenotime substitution, Am. Mineral., 86, 681–689, https://doi.org/10.2138/am-2001-5-608, 2001.

Förster, H.-J.: Composition and origin of intermediate solid solutions in the system thorite–xenotime–zircon–coffinite, Lithos, 88, 35–55, https://doi.org/10.1016/j.lithos.2005.08.003, 2006.

Fouillac, A. M., Kosakevitch, A., Merceron, T., Meunier, A., and Rossi, P.: Comportement des fluides dans l'évolution magmatique puis hydrothermale du granite à Ta, Nb, Li de Beauvoir, d'après la géochimie isotopique de l'oxygène et de l'hydrogène, Géologie Fr., 2–3 279–293, 1987.

Friedrich, M. H., Cuney, M., and Poty, B.: Uranium Geochemistry in Peraluminous Leucogranites, Uranium, 3, 353–385, 1987.

Fuchs, L. and Gebert, E.: X-ray studies of synthetic coffinite, thorite and uranothorites, Am. Mineral. J. Earth Planet. Mater., 43, 243–248, 1958.

Gagny, C.: Organisation séquentielle évolutive des intrusions successives du granite de Beauvoir dans son caisson: arguments géochimiques, Géologie Fr., 2–3, 199–208, 1987.

Geisler, T., Pidgeon, R. T., Van Bronswijk, W., and Kurtz, R.: Transport of uranium, thorium, and lead in metamict zircon under low-temperature hydrothermal conditions, Chem. Geol., 191, 141–154, https://doi.org/10.1016/S0009-2541(02)00153-5, 2002.

Geisler, T., Pidgeon, R. T., Kurtz, R., Van Bronswijk, W., and Schleicher, H.: Experimental hydrothermal alteration of partially metamict zircon, Am. Mineral., 88, 1496–1513, https://doi.org/10.2138/am-2003-1013, 2003a.

Geisler, T., Rashwan, A. A., Rahn, M. K. W., Poller, U., Zwingmann, H., Pidgeon, R. T., Schleicher, H., and Tomaschek, F.: Low-temperature hydrothermal alteration of natural metamict zircons from the Eastern Desert, Egypt, Mineral. Mag., 67, 485–508, https://doi.org/10.1180/0026461036730112, 2003b.

Geisler, T., Trachenko, K., Ríos, S., Dove, M., and Salje, E. K. H.: Impact of self-irradiation damage on the aqueous durability of zircon ($ZrSiO_4$): implications for its suitability as a nuclear waste form, J. Phys. Condens. Matter, 15, L597–L605, https://doi.org/10.1088/0953-8984/15/37/L07, 2003c.

Geisler, T., Burakov, B. E., Zirlin, V., Nikolaeva, L., and Pöml, P.: A Raman spectroscopic study of high-uranium zircon from the Chernobyl "lava," Eur. J. Mineral., 17, 883–894, https://doi.org/10.1127/0935-1221/2005/0017-0883, 2006.

Geisler, T., Schaltegger, U., and Tomaschek, F.: Re-equilibration of Zircon in Aqueous Fluids and Melts, Elements, 3, 43–50, https://doi.org/10.2113/gselements.3.1.43, 2007.

Gerstenberger, H. and Haase, G.: A highly effective emitter substance for mass spectrometric Pb isotope ratio determinations, Chem. Geol., 136, 309–312, https://doi.org/10.1016/S0009-2541(96)00033-2, 1997.

Gillespie, J., Klein, B. Z., Moore, J., Müntener, O., and Baumgartner, L. P.: A dendritic growth mechanism for producing oscillatory zoning in igneous zircon, Geology, 53, 171–175, https://doi.org/10.1130/G52641.1, 2024.

Grolier, J.: Contribution à l'étude géologique des séries crystallophylliennes inverses du massif Central français: la série de la Sioule (Puy de Dôme, Allier), Mém BRGM, 64, 163pp., 1971.

Han, J., Hanchar, J. M., Pan, Y., Hollings, P., and Chen, H.: Hydrothermal alteration, not metamictization, is the main trigger for modifying zircon in highly evolved granites, Geol. Soc. Am. Bull., 136, 1878–1888, https://doi.org/10.1130/B36996.1, 2023.

Hanchar, J. M., Finch, R. J., Hoskin, P. W., Watson, E. B., Cherniak, D. J., and Mariano, A. N.: Rare earth elements in synthetic zircon: Part 1. Synthesis, and rare earth element and phosphorus doping, Am. Mineral., 86, 667–680, https://doi.org/10.2138/am-2001-5-607, 2001.

Harlaux, M., Mercadier, J., Bonzi, W. M.-E., Kremer, V., Marignac, C., and Cuney, M.: Geochemical Signature of Magmatic-Hydrothermal Fluids Exsolved from the Beauvoir Rare-Metal Granite (Massif Central, France): Insights from LA-ICPMS Analysis of Primary Fluid Inclusions, Geofluids, 2017, 1–25, https://doi.org/10.1155/2017/1925817, 2017.

Harlaux, M., Blein, O., Ballouard, C., Kontak, D. J., Thiéblemont, D., Dabosville, A., and Gourcerol, B.: Geochemical footprints of peraluminous rare-metal granites and pegmatites in the northern French Massif Central and implications for exploration targeting, Ore Geol. Rev., 176, 106409, https://doi.org/10.1016/j.oregeorev.2024.106409, 2025.

Hetherington, C. J. and Harlov, D. E.: Metasomatic thorite and uraninite inclusions in xenotime and monazite from granitic pegmatites, Hidra anorthosite massif, southwestern Norway: Mechanics and fluid chemistry, Am. Mineral., 93, 806–820, https://doi.org/10.2138/am.2008.2635, 2008.

Holland, H. D. and Gottfried, D.: The effect of nuclear radiation on the structure of zircon, Acta Crystallogr., 8, 291–300, https://doi.org/10.1107/S0365110X55000947, 1955.

Hoskin, P. W.: Trace-element composition of hydrothermal zircon and the alteration of Hadean zircon from the Jack Hills, Australia, Geochim. Cosmochim. Ac., 69, 637–648, https://doi.org/10.1016/j.gca.2004.07.006, 2005.

Hoskin, P. W. O. and Schaltegger, U.: The Composition of Zircon and Igneous and Metamorphic Petrogenesis, Rev. Mineral. Geochem., 53, 27–62, https://doi.org/10.2113/0530027, 2003.

Hoskin, P. W. O., Kinny, P. D., Wyborn, D., and Chappell, B. W.: Identifying Accessory Mineral Saturation during Differentiation in Granitoid Magmas: an Integrated Approach, J. Petrol., 41, 1365–1396, https://doi.org/10.1093/petrology/41.9.1365, 2000.

Jaffey, A., Flynn, K., Glendenin, L., Bentley, W. T., and Essling, A.: Precision measurement of half-lives and specific activities of U 235 and U 238, Phys. Rev. C, 4, 1889, https://doi.org/10.1103/PhysRevC.4.1889, 1971.

Jia, L., Wu, C.-Z., Lei, R.-X., Brzozowski, M. J., Wang, Y.-T., Qian, Z.-Z., and Deng, X.-H.: Geochronology and geochemistry of zircon and columbite–tantalite group minerals from the Weilasituo Sn–polymetallic deposit, northeastern China: Implications for the relationship between mineralization and the magmatic–hydrothermal transition, Ore Geol. Rev., 168, 106047, https://doi.org/10.1016/j.oregeorev.2024.106047, 2024.

Kryza, R., Schaltegger, U., Oberc-Dziedzic, T., Pin, C., and Ovtcharova, M.: Geochronology of a composite granitoid pluton: a high-precision ID-TIMS U–Pb zircon study of the Variscan Karkonosze Granite (SW Poland), Int. J. Earth Sci., 103, 683–696, https://doi.org/10.1007/s00531-013-0995-0, 2014.

Lafuente, B., Downs, R. T., Yang, H., and Stone, N.: The power of databases: the RRUFF project, Highlights Mineral. Crystallogr., edited by: Armbruster, T. and Danisi, R. M., Berl. Ger. W Gruyter, 1–30, https://doi.org/10.1515/9783110417104-003, 2015.

Lanari, P., Vidal, O., De Andrade, V., Dubacq, B., Lewin, E., Grosch, E. G., and Schwartz, S.: XMapTools: A MATLAB© - based program for electron microprobe X-ray image processing and geothermobarometry, Computers & Geosciences, 62, 227–240, https://doi.org/10.1016/j.cageo.2013.08.010, 2014.

Lanari, P., Vho, A., Bovay, T., Airaghi, L., & Centrella, S.: Quantitative compositional mapping of mineral phases by electron probe micro-analyser, Geological Society, London, Special Publications, 478, 39–63, https://doi.org/10.1144/SP478.4, 2019.

Large, S. J. E., Wotzlaw, J.-F., Guillong, M., von Quadt, A., and Heinrich, C. A.: Resolving the timescales of magmatic and hydrothermal processes associated with porphyry deposit formation using zircon U–Pb petrochronology, Geochronology, 2, 209–230, https://doi.org/10.5194/gchron-2-209-2020, 2020.

Le Roux, L. and Glendenin, L.: Half-life of ^{232}Th, in: Proceedings of the National Meeting on Nuclear Energy, Pretoria, South Africa, 5–8 April 1963, 83–94, 1963.

Leuthold, J., Müntener, O., Baumgartner, L. P., Putlitz, B., Ovtcharova, M., and Schaltegger, U.: Time resolved construction of a bimodal laccolith (Torres del Paine, Patagonia), Earth Planet. Sc. Lett., 325–326, 85–92, https://doi.org/10.1016/j.epsl.2012.01.032, 2012.

Linnen, R. L. and Keppler, H.: Melt composition control of Zr/Hf fractionation in magmatic processes, Geochim. Cosmochim. Ac., 66, 3293–3301, https://doi.org/10.1016/S0016-7037(02)00924-9, 2002.

Linnen, R. L., Van Lichtervelde, M., and Cerny, P.: Granitic Pegmatites as Sources of Strategic Metals, Elements, 8, 275–280, https://doi.org/10.2113/gselements.8.4.275, 2012.

Liu, X.-H., Li, B., Lai, J.-Q., and Jiang, S.-Y.: Multistage in situ fractional crystallization of magma produced a unique rare metal enriched quartz-zinnwaldite-topaz rock, Ore Geol. Rev., 151, 105203, https://doi.org/10.1016/j.oregeorev.2022.105203, 2022.

London, D.: The application of experimental petrology to the genesis and crystallization of granitic pegmatites, Can. Mineral., 30, 499–540, 1992.

London, D.: Ore-forming processes within granitic pegmatites, Ore Geol. Rev., 101, 349–383, https://doi.org/10.1016/j.oregeorev.2018.04.020, 2018.

López-Moro, F. J., Díez-Montes, A., Timón-Sánchez, S. M., Llorens-González, T., and Sánchez-García, T.: Peraluminous Rare Metal Granites in Iberia: Geochemical, Mineralogical, Geothermobarometric, and Petrogenetic Constraints, Minerals, 14, 249, https://doi.org/10.3390/min14030249, 2024.

Lu, T.-Y., He, Z.-Y., and Klemd, R.: Different magma differentiation processes of post-onset collision adakitic rocks in the Gangdese Batholith: Evidence from zircon trace elements, Chem. Geol., 620, 121345, https://doi.org/10.1016/j.chemgeo.2023.121345, 2023.

Ludwig, K. R.: ISOPLOT: a plotting and regression program for radiogenic-isotope data; version 2.53, US Geological Survey Open-file Report 91-445, 39 pp., https://doi.org/10.3133/ofr91445, 1991.

Ludwig, K. R.: On the Treatment of Concordant Uranium-Lead Ages, Geochim. Cosmochim. Ac., 62, 665–676, https://doi.org/10.1016/S0016-7037(98)00059-3, 1998.

McKanna, A. J., Schoene, B., and Szymanowski, D.: Geochronological and geochemical effects of zircon chemical abrasion: insights from single-crystal stepwise dissolution experiments, Geochronology, 6, 1–20, https://doi.org/10.5194/gchron-6-1-2024, 2024.

McLean, N. M., Bowring, J. F., and Bowring, S. A.: An algorithm for U-Pb isotope dilution data reduction and uncertainty propagation, Geochem. Geophys. Geosyst., 12, 1–26, https://doi.org/10.1029/2010GC003478, 2011.

McLean, N. M., Condon, D. J., Schoene, B., and Bowring, S. A.: Evaluating Uncertainties in the Calibration of Isotopic Reference Materials and Multi-Element Isotopic Tracers (EARTHTIME Tracer Calibration Part II), Geochem. Cosmochim. Ac., 164, 481–501, https://doi.org/10.1016/j.gca.2015.02.040, 2015.

Melleton, J., Gloaguen, E., and Frei, D.: Rare-Elements (Li-Be-Ta-Sn-Nb) Magmatism in the European Variscan Belt, a Review, Proceedings, 2, 807–810, 2015.

Merceron, T., Vieillard, P., Fouillac, A.-M., and Meunier, A.: Hydrothermal alterations in the Echassières granitic cupola (Massif central, france), Contrib. Mineral. Petrol., 112, 279–292, https://doi.org/10.1007/BF00310461, 1992.

Mezger, K. and Krogstad, E.: Interpretation of discordant U-Pb zircon ages: An evaluation, J. Metamorph. Geol., 15, 127–140, https://doi.org/10.1111/j.1525-1314.1997.00008.x, 1997.

Michaud, J. A.-S., Gumiaux, C., Pichavant, M., Gloaguen, E., and Marcoux, E.: From magmatic to hydrothermal Sn-Li-(Nb-Ta-W) mineralization: The Argemela area (central Portugal), Ore Geol. Rev., 116, 103215, https://doi.org/10.1016/j.oregeorev.2019.103215, 2020.

Monnier, L.: Utilisation de la signature LA-ICPMS des quartz et des micas pour la reconstruction du fonctionnement d'un système magmatique et hydrothermal polyphasé. Application au complexe Sn-W d'Echassières (Massif Central, France), Doctoral thesis, Université Paul Sabatier, Toulouse, 386 pp., 2018.

Monnier, L., Salvi, S., Jourdan, V., Sall, S., Bailly, L., Melleton, J., and Béziat, D.: Contrasting fluid behavior during two styles of greisen alteration leading to distinct wolframite mineralizations: The Echassières district (Massif Central, France), Ore Geol. Rev., 124, 103648, https://doi.org/10.1016/j.oregeorev.2020.103648, 2020.

Monnier, L., Salvi, S., Melleton, J., Lach, P., Pochon, A., Bailly, L., Béziat, D., and De Parseval, P.: Mica trace-element signatures: Highlighting superimposed W-Sn mineralizations and fluid sources, Chem. Geol., 600, 120866, https://doi.org/10.1016/j.chemgeo.2022.120866, 2022.

Monnier, L., Laurent, O., Salvi, S., Bernard, C., Leisen, M., Estrade, G., Parseval, P. de, Josse, C., Descamps-Mandine, A., Duan, Z., Gouy, S., Carmo, C. P. do, and Dusséaux, C.: Of zircons and zircons: The tumultuous story of Zr-Hf and REE during cooling of peralkaline granites, Geochim. Cosmochim. Ac., 402, 250–276, https://doi.org/10.1016/j.gca.2025.05.039, 2025.

Murakami, T., Chakoumakos, B. C., Ewing, R. C., Lumpkin, G. R., and Weber, W. J.: Alpha-decay event damage in zircon, Am. Mineral., 76, 1510–1532, 1991.

Nasdala, L., Pidgeon, R., Wolf, D., and Irmer, G.: Metamictization and U-Pb isotopic discordance in single zircons: a combined Raman microprobe and SHRIMP ion probe study, Mineral. Petrol., 62, 1, https://doi.org/10.1007/BF01173760, 1998.

Nasdala, L., Wenzel, M., Vavra, G., Irmer, G., Wenzel, T., and Kober, B.: Metamictisation of natural zircon: accumulation versus thermal annealing of radioactivity-induced damage, Contrib. Mineral. Petrol., 141, 125–144, https://doi.org/10.1007/s004100000235, 2001.

Neves, J. C., Nunes, J. L., and Sahama, T. G.: High hafnium members of the zircon-hafnon series from the granite pegmatites of

Zambézia, Mozambique, Contrib. Mineral. Petrol., 48, 73–80, https://doi.org/10.1007/BF00399111, 1974.

Ohnenstetter, D. and Piantone, P.: Géochimie et évolutions des minéraux du groupe des columbo-tantalites et des minéraux du groupe du pyrochlore du sondage GPF-1 Echassières (Allier), Doc. BRGM, 124, 113–163, 1988.

Paul, A. N., Spikings, R. A., Chew, D., and Daly, J. S.: The effect of intra-crystal uranium zonation on apatite U-Pb thermochronology: A combined ID-TIMS and LA-MC-ICP-MS study, Geochim. Cosmochim. Ac., 251, 15–35, https://doi.org/10.1016/j.gca.2019.02.013, 2019.

Paul, A. N., Spikings, R. A., and Gaynor, S. P.: U-Pb ID-TIMS reference ages and initial Pb isotope compositions for Durango and Wilberforce apatites, Chem. Geol., 586, 120604, https://doi.org/10.1016/j.chemgeo.2021.120604, 2021.

Pérez-Soba, C., Villaseca, C., Orejana, D., and Jeffries, T.: Uranium-rich accessory minerals in the peraluminous and perphosphorous Belvís de Monroy pluton (Iberian Variscan belt), Contrib. Mineral. Petrol., 167, 1008, https://doi.org/10.1007/s00410-014-1008-4, 2014.

Pichavant, M.: Experimental crystallization of the Beauvoir granite as a model for the evolution of Variscan rare metal magmas, J. Petrol., 63, 1–28, https://doi.org/10.1093/petrology/egac120, 2022.

Pichavant, M., Kontak, D. J., Herrera, J. V., and Clark, A. H.: The Miocene-Pliocene Macusani Volcanics, SE Peru, Contrib. Mineral. Petrol., 300–324, https://doi.org/10.1007/BF00379741, 1988.

Pin, C.: Sr-Nd isotopic study of igneous and metasedimentary enclaves is some hercynian granitoids from the Massif Central, France. In: Didier, J., Barbarin, B. (Eds.), Enclaves and Granite Petrology (Developments in Petrology), Elsevier, 13, 33–343, 1991.

Popov, D., Spikings, R., Paul, A. N., Ovtcharova, M., Chiaradia, M., Kutzschbach, M., Ulianov, A., O'Sullivan, G., Chew, D., Kouzmanov, K., Badenszki, E., Daly, J. S., and Davies, J. H. F. L.: Excess 40Ar in Alkali Feldspar and 206,207Pb in Apatite Caused by Fluid-Induced Recrystallisation in a Semi-Closed Environment in Proterozoic (Meta)Granites of the Mt Isa Inlier, NE Australia, Geosciences, 14, 358, https://doi.org/10.3390/geosciences14120358, 2024.

Popov, D. V. and Spikings, R. A.: Numerical Modelling of Radiogenic Ingrowth and Diffusion of Pb in Apatite Inclusions with Variable Shape and U-Th Zonation, Minerals, 11, 364, https://doi.org/10.3390/min11040364, 2021.

Popov, D. V., Spikings, R. A., Scaillet, S., O'Sullivan, G., Chew, D., Badenszki, E., Daly, J. S., Razakamanana, T., and Davies, J. H. F. L.: Diffusion and fluid interaction in Itrongay pegmatite (Madagascar): Evidence from in situ 40Ar/39Ar dating of gem-quality alkali feldspar and U Pb dating of protogenetic apatite inclusions, Chem. Geol., 556, 119841, https://doi.org/10.1016/j.chemgeo.2020.119841, 2020.

Raimbault, L. and Burnol, L.: The Richemont rhyolite dyke, Massif central, France: A subvolcanic equivalent of rare-metal granites., Can. Mineral., 36, 265–282, 1998.

Raimbault, L., Cuney, M., Azencott, C., Duthou, J.-L., and Joron, J. L.: Geochemical evidence for a multistage magmatic genesis of Ta-Sn-Li mineralization in the granite at Beauvoir, French Massif Central, Econ. Geol., 90, 548–576, https://doi.org/10.2113/gsecongeo.90.3.548, 1995.

Ramakrishnan, S., Gokhale, K., and Subbarao, E.: Solid solubility in the system zircon-hafnon, Mater. Res. Bull., 4, 323–327, https://doi.org/10.1016/0025-5408(69)90036-1, 1969.

René, M.: Composition of coexisting zircon and xenotime in rare-metal granites from the Krušné Hory/Erzgebirge Mts. (Saxothuringian Zone, Bohemian Massif), Mineral. Petrol., 108, 551–569, https://doi.org/10.1007/s00710-013-0318-y, 2014.

Ribeiro, H. B., Guedes, K. J., Pinheiro, M. V. B., Greulich-Weber, S., and Krambrock, K.: About the blue and green colours in natural fluorapatite, Phys. Status Solidi C, 2, 720–723, https://doi.org/10.1002/pssc.200460274, 2005.

Rocher, O., Ballouard, C., Richard, A., Monnier, L., Carr, P. A., Laurent, O., Khebabza, Y., Lecomte, A., Bouden, N., Villeneuve, J., Barré, B., Fullenwarth, P., Leisen, M., and Mercadier, J.: Unravelling the magmatic and hydrothermal evolution of rare-metal granites through apatite geochemistry and geochronology: the Variscan Beauvoir granite (French Massif Central), Chem. Geol., 670, 122400, https://doi.org/10.1016/j.chemgeo.2024.122400, 2024.

Romer, R. L. and Lüders, V.: Direct dating of hydrothermal W mineralization: U–Pb age for hübnerite (MnWO4), Sweet Home Mine, Colorado, Geochim. Cosmochim. Ac., 70, 4725–4733, https://doi.org/10.1016/j.gca.2006.07.003, 2006.

Romer, R. L. and Smeds, S.-A.: Implications of U-Pb ages of columbite-tantalites from granitic pegmatites for the Palaeoproterozoic accretion of 1.90–1.85 Ga magmatic arcs to the Baltic Shield, Precambrian Res., 67, 141–158, https://doi.org/10.1016/0301-9268(94)90008-6, 1994.

Rossi, Autran, A., Azencott, C., Burnol, L., Cuney, M., Johan, V., Kosakevitch, A., Ohnenstetter, D., Monier, G., Piantone, P., Raimbault, L., and Viallefond, L.: Logs pétrographique et géochimique du granite de Beauvoir dans le sondage "Echassières I", Minéralogie et géochimie comparées, Géologie Fr., 2–3, 111–135, 1987.

Salje, E., Chrosch, J., and Ewing, R.: Is "metamictization" of zircon a phase transition?, Am. Mineral., 84, 1107–1116, 1999.

Scaillet, B., Pichavant, M., and Roux, J.: Experimental crystallization of leucogranite magmas, J. Petrol., 36, 663–705, https://doi.org/10.1093/petrology/36.3.663, 1995.

Schaltegger, U.: Hydrothermal zircon, Elements, 3, 51–79, https://doi.org/10.2113/gselements.3.1.51, 2007.

Schaltegger, U., Ovtcharova, M., Gaynor, S. P., Schoene, B., Wotzlaw, J.-F., Davies, J. F. H. L., Farina, F., Greber, N. D., Szymanowski, D., and Chelle-Michou, C.: Long-term repeatability and interlaboratory reproducibility of high-precision ID-TIMS U–Pb geochronology, J. Anal. At. Spectrom., 36, 1466–1477, https://doi.org/10.1039/D1JA00116G, 2021.

Schaltegger, U., Ovtcharova, M., and Schoene, B.: High-precision CA-ID-TIMS U-Pb geochronology of zircon: Materials, methods, and interpretations, Methods Appl. Geochronol., 19–52, https://doi.org/10.1016/B978-0-443-18803-9.00012-2, 2024.

Schmitz, M. D. and Schoene, B.: Derivation of isotope ratios, errors, and error correlations for U-Pb geochronology using ^{205} Pb-^{235} U-(^{233} U)-spiked isotope dilution thermal ionization mass spectrometric data, Geochem. Geophys. Geosys., 8, 2006GC001492, https://doi.org/10.1029/2006GC001492, 2007.

Schoene, B., Schaltegger, U., Brack, P., Latkoczy, C., Stracke, A., and Günther, D.: Rates of magma differentiation and emplacement in a ballooning pluton recorded by U–Pb TIMS-TEA, Adamello batholith, Italy, Earth Planet. Sc. Lett., 355–356, 162–173, https://doi.org/10.1016/j.epsl.2012.08.019, 2012.

Shannon, R. D.: Revised effective ionic radii and systematic studies of interatomic distances in halides and chalcogenides, Found. Crystallogr., 32, 751–767, https://doi.org/10.1107/S0567739476001551, 1976.

Speer, J. A.: Zircon, Mineral. Soc. Am. Rev. Mineral., 5, 67–112, 1980.

Speer, J. A. and Cooper, B. J.: Crystal structure of synthetic hafnon, $HfSiO_4$, comparison with zircon and the actinide orthosilicates, Am. Mineral., 67, 804–808, 1982.

Stacey, J. S. and Kramers, J. D.: Approximation of terrestrial lead isotope evolution by a two-stage model, Earth Planet. Sc. Lett., 26, 207–221, https://doi.org/10.1016/0012-821X(75)90088-6, 1975.

Švecová, E., Èopjaková, R., Losos, Z., Škoda, R., Nasdala, L., and Cícha, J.: Multi-stage evolution of xenotime–(Y) from Písek pegmatites, Czech Republic: an electron probe micro-analysis and Raman spectroscopy study, Mineral. Petrol., 110, 747–765, https://doi.org/10.1007/s00710-016-0442-6, 2016.

Tanabe, K. and Hiraishi, J.: Correction of finite slit width effects on Raman line widths, Spectrochim. Acta Part Mol. Spectrosc., 36, 341–344, https://doi.org/10.1016/0584-8539(80)80141-3, 1980.

Troch, J., Ellis, B. S., Schmitt, A. K., Bouvier, A.-S., and Bachmann, O.: The dark side of zircon: textural, age, oxygen isotopic and trace element evidence of fluid saturation in the subvolcanic reservoir of the Island Park-Mount Jackson Rhyolite, Yellowstone (USA), Contrib. Mineral. Petrol., 173, 54, https://doi.org/10.1007/s00410-018-1481-2, 2018.

Uher, P. and Černý, P.: Zircon in Hercynian granitic pegmatites of the western Carpathians, Slovakia, Geol. Carpathica, 49, 261–270, 1998.

Ushakov, S. V., Gong, W., Yagovkina, M. M., Helean, K. B., Lutze, W., and Ewing, R. C.: Solid solutions of Ce, U and Th in zircon, Ceram. Trans., 93, 357–363, 1999.

Van Lichtervelde, M., Salvi, S., Beziat, D., and Linnen, R. L.: Textural Features and Chemical Evolution in Tantalum Oxides: Magmatic Versus Hydrothermal Origins for Ta Mineralization in the Tanco Lower Pegmatite, Manitoba, Canada, Econ. Geol., 102, 257–276, https://doi.org/10.2113/gsecongeo.102.2.257, 2007.

Van Lichtervelde, M., Melcher, F., and Wirth, R.: Magmatic vs. hydrothermal origins for zircon associated with tantalum mineralization in the Tanco pegmatite, Manitoba, Canada, Am. Mineral., 94, 439–450, https://doi.org/10.2138/am.2009.2952, 2009.

Wang, X., Griffin, W. L., and Chen, J.: Hf contents and Zr/Hf ratios in granitic zircons, Geochem. J., 44, 65–72, https://doi.org/10.2343/geochemj.1.0043, 2010.

Wark, D. A. and Miller, C. F.: Accessory mineral behavior during differentiation of a granite suite: monazite, xenotime and zircon in the Sweetwater Wash pluton, southeastern California, U.S.A., Chem. Geol., 110, 49–67, https://doi.org/10.1016/0009-2541(93)90247-G, 1993.

Watson, E. B., Wark, D. A., and Thomas, J. B.: Crystallization thermometers for zircon and rutile, Contrib. Mineral. Petrol., 151, 413–433, https://doi.org/10.1007/s00410-006-0068-5, 2006.

Widmann, P., Davies, J. H. F. L., and Schaltegger, U.: Calibrating chemical abrasion: Its effects on zircon crystal structure, chemical composition and U Pb age, Chem. Geol., 511, 1–10, https://doi.org/10.1016/j.chemgeo.2019.02.026, 2019.

Wyllie, P. J. and Tuttle, O. F.: Experimental investigation of silicate systems containing two volatile components. Part 3. The effect of SO_3, P_2O_5, HCl, and Li_2O, in addition to H_2O, on the Melting Temperatures of Albite and Granite., Am. J. Sci., 262, 930–939, 1964.

Yang, M., Yang, Y.-H., Romer, R. L., Che, X.-D., Wang, R.-C., Wu, F.-Y., Fei, G.-C., Deng, Y., and Wu, T.: Characterization of reference materials for in situ U–Pb dating of columbite group minerals by LA-ICP-MS, J. Anal. At. Spectrom., 38, 1816–1829, https://doi.org/10.1039/D3JA00162H, 2023.

Zaraisky, G. P., Aksyuk, A. M., Devyatova, V. N., Udoratina, O. V., and Chevychelov, V. Yu.: Zr/Hf ratio as an indicator of fractionation of rare-metal granites by the example of the Kukulbei complex, eastern Transbaikalia, Petrology, 16, 710–736, https://doi.org/10.1134/S0869591108070047, 2008.

Zoheir, B., Lehmann, B., Emam, A., Radwan, A., Zhang, R., Bain, W. M., Steele-MacInnis, M., and Nolte, N.: Extreme fractionation and magmatic–hydrothermal transition in the formation of the Abu Dabbab rare-metal granite, Eastern Desert, Egypt, Lithos, 352–353, 105329, https://doi.org/10.1016/j.lithos.2019.105329, 2020.